Ram-pressure stripped radio tail and two ULXs in the spiral galaxy HCG 97b

Dan Hu, Michal Zajaček, Norbert Werner, Romana Grossová, Pavel Jáchym, Ian D. Roberts, Alessandro Ignesti, Jeffrey D. P. Kenney, Tomáš Plšek, Jean-Paul Breuer, et al.

Monthly Notices of the ROYAL ASTRONOMICAL SOCIETY

MNRAS **527,** 1062–1080 (2024) https://doi.org/10.1093/mnras/stad3219
Advance Access publication 2023 October 23

Ram-pressure stripped radio tail and two ULXs in the spiral galaxy HCG 97b

Dan Hu [1]★ Michal Zajaček,[1] Norbert Werner [1] Romana Grossová,[1,2] Pavel Jáchym,[2] Ian D. Roberts [3] Alessandro Ignesti,[4] Jeffrey D.P. Kenney,[5] Tomáš Plšek [1] Jean-Paul Breuer [1] Timothy Shimwell,[3,6] Cyril Tasse,[7,8] Zhenghao Zhu[9] and Linhui Wu[9]

[1]*Department of Theoretical Physics and Astrophysics, Faculty of Science, Masaryk University, Kotlářská 2, 611 37 Brno, Czech Republic*
[2]*Astronomical Institute of the Czech Academy of Sciences, Boční II 1401, 141 00 Prague, Czech Republic*
[3]*Leiden Observatory, Leiden University, PO Box 9513, 2300 RA Leiden, The Netherlands*
[4]*INAF – Astronomical Observatory of Padova, vicolo dell'Osservatorio 5, I-35122 Padova, Italy*
[5]*Department of Astronomy, Yale University, New Haven, CT 06511, USA*
[6]*ASTRON, The Netherlands Institute for Radio Astronomy, Postbus 2, 7990 AA Dwingeloo, The Netherlands*
[7]*GEPI & ORN, Observatoire de Paris, Université PSL, CNRS, 5 Place Jules Janssen, F-92190 Meudon, France*
[8]*Department of Physics & Electronics, Rhodes University, PO Box 94, 6140 Grahamstown, South Africa*
[9]*Shanghai Astronomical Observatory, Chinese Academy of Sciences, Nandan Road 80, 200030 Shanghai, China*

Accepted 2023 October 17. Received 2023 October 16; in original form 2023 April 24

ABSTRACT

We report *LOFAR* and *Very Large Array* (*VLA*) detections of extended radio emission in the spiral galaxy HCG 97b, hosted by an X-ray bright galaxy group. The extended radio emission detected at 144 MHz, 1.4 GHz, and 4.86 GHz is elongated along the optical disc and has a tail that extends 27 kpc in projection towards the centre of the group at GHz frequencies or 60 kpc at 144 MHz. Chandra X-ray data show two off-nuclear ultra-luminous X-ray sources (ULXs), with the farther one being a plausible candidate for an accreting intermediate-mass black hole (IMBH). The asymmetry observed in both CO emission morphology and kinematics indicates that HCG 97b is undergoing ram-pressure stripping, with the leading side at the south-eastern edge of the disc. Moreover, the *VLA* 4.86 GHz image reveals two bright radio blobs near one ULX, aligning with the disc and tail, respectively. The spectral indices in the disc and tail are comparable and flat ($\alpha > -1$), suggesting the presence of recent outflows potentially linked to ULX feedback. This hypothesis gains support from estimates showing that the bulk velocity of the relativistic electrons needed for transport from the disc to the tail is approximately $\sim$1300 km s^{-1}. This velocity is much higher than those observed in ram-pressure stripped galaxies (100−600 km s^{-1}), implying an alternative mechanism aiding the stripping process. Therefore, we conclude that HCG 97b is subject to ram pressure, with the formation of its stripped radio tail likely influenced by the putative IMBH activities.

Key words: galaxies: individual: HCG 97b – galaxies: interactions – radio continuum: galaxies.

1 INTRODUCTION

The properties of galaxies within a dense environment are influenced via various mechanisms, such as mergers (e.g. Spitzer & Baade 1951; Mihos & Hernquist 1994a,b; Springel 2000; Misquitta et al. 2023), tidal interactions (e.g. Byrd & Valtonen 1990; Valluri 1993; Mayer et al. 2006; Chung et al. 2007; Łokas 2020), ram-pressure stripping (e.g. Gunn & Gott 1972; Quilis, Moore & Bower 2000; Jáchym et al. 2014; Roberts et al. 2021a), and viscous stripping (e.g. Nulsen 1982; Quilis, Moore & Bower 2000; Roediger et al. 2015). Mergers and tidal interactions are primarily gravitational effects that affect both stellar and gas components of a galaxy, while the other two are predominantly hydrodynamical effects that only influence the gas content of the galaxy. Ram-pressure stripping can effectively remove the interstellar medium (ISM) from galaxies that are falling into cluster environments, leading to the subsequent formation of gas tails. The most extreme examples of galaxies undergoing intense ram-pressure stripping are so-called jellyfish galaxies (e.g. Smith et al. 2010; Ebeling, Stephenson & Edge 2014; Fumagalli et al. 2014; and see Boselli, Fossati & Sun 2022, for a review).

Extended, one-sided gas tails from ram-pressure stripped galaxies were observed in some galaxy clusters via Hα (e.g. Gavazzi et al. 2001; Sun, Donahue & Voit 2007; Gavazzi et al. 2017), H I (e.g. Kenney et al. 2014; Deb et al. 2020), CO (e.g. Jáchym et al. 2014, 2019), X-ray emission (e.g. Sun et al. 2006, 2010; Poggianti et al. 2019), and radio continuum emission (Gavazzi & Jaffe 1987; Murphy et al. 2009; Vollmer et al. 2009, 2013; Müller et al. 2021; Ignesti et al. 2022; Roberts et al. 2022a). In general, radio continuum emission in ram-pressure stripped galaxies is mainly caused by non-thermal synchrotron emission of relativistic cosmic ray electrons (CRe), which are accelerated by supernovae (SNe) shocks [see e.g. Condon

★ E-mail: hudan.bazhaoyu@gmail.com

(1992) for a review]. These relativistic CRe are then stripped from the galaxy by ram pressure due to the relative motion between the galaxy and the ambient environment and possibly further re-accelerated by turbulence, intracluster medium (ICM) shocks, or new SNe. As such, radio continuum emission presents a valuable complementary tool for studying the phenomenon of ram-pressure stripped tails.

The process of ram-pressure stripping is generally observed in galaxy clusters due to their high ICM densities and large infall velocities. However, the ram-pressure exerted by the intragroup medium (IGrM) is commonly considered to be inefficient, resulting in a stripping process extended over a longer time-scale (∼3 Gyr), as supported by cosmological hydrodynamical simulation performed by Oman et al. (2021). Despite this, evidence of ram-pressure stripping in galaxy groups is still observed (e.g. Davis et al. 1997; Sivakoff, Sarazin & Carlin 2004; Kantharia et al. 2005; Machacek et al. 2005; Rasmussen, Ponman & Mulchaey 2006). Recently, the number of known ram-pressure stripped galaxies in galaxy groups was increased as Roberts et al. (2021b) identified 60 jellyfish galaxies with extended, asymmetric radio continuum tails in low-mass systems with the *LOFAR* Two-metre Sky Survey (LoTSS; Shimwell et al. 2017, 2022), that has a high sensitivity (∼0.1 mJy beam^{-1}) at low frequency (144 MHz). However, it should be noted that ram-pressure stripping might not be the only mechanism explaining the gas morphology seen in these low-mass systems, which might also be affected by tidal interaction as suggested by the aforementioned authors or by active galactic nucleus (AGN) activity (e.g. Poggianti et al. 2017).

To further investigate the gas removal from galaxies in the group environment, we conducted a multiwavelength study of the spiral galaxy HCG 97b (alternative name IC5359), which resides at ∼100 kpc south-east of the central galaxy HCG 97a (IC5357) of the galaxy group HCG 97. This galaxy is moderately inclined, appearing close to edge-on but not completely perpendicular to our line of sight. The bulge-to-total luminosity ratio is ∼0.08 using the SDSS g-band data (Bizyaev et al. 2014). The mean Heliocentric radial velocity of HCG 97b is 6940 ± 74 kms^{-1} (Hickson et al. 1992), and the stellar mass of HCG 97b is ∼1.7 × 10^{10} M$_\odot$ estimated by using *K*s-band luminosity (Bitsakis et al. 2011). The apparent diameter D_{25} (defined by the isophote at the brightness of 25 mag arcsec^{-2} in the *B* band) of the spiral galaxy HCG 97b is 1.23 ± 0.11 arcmin (from HyperLeda database;[1] Makarov et al. 2014), corresponding to 35 ± 3.1 kpc (1 arcmin ≈ 27 kpc), implying it is a large spiral galaxy comparable to our Milky Way (D_{25} = 26.8 ± 1.1 kpc; Goodwin, Gribbin & Hendry 1998). The results of this work suggest the presence of two off-nuclear X-ray sources that are likely ultra-luminous X-ray sources (ULXs), as well as an extended, one-sided radio tail that is being stripped by ram pressure resulting from the galaxy–IGrM interaction. One of the ULXs may be a candidate for an activated intermediate-mass black hole (IMBH) and has a potential link with the nearby radio tail. Therefore, HCG 97b presents an ideal case for studying ram-pressure stripped galaxies in the group environment and investigating the potential contribution of ULXs/IMBH to the enhancement of ram-pressure stripping.

Throughout this paper, we assume the standard flat ΛCDM cosmology with parameters H_0 = 70 km s^{-1} Mpc^{-1} and Ω_m = 1 − Ω_Λ = 0.27. At the redshift of HCG 97b (z = 0.022), these values result in a scale of ∼27 kpc arcmin^{-1} and a luminosity distance of 97 Mpc. For the radio spectral index α, we use the convention $S_\nu \propto \nu^\alpha$, where S_ν is the flux density at the frequency of ν.

[1] http://leda.univ-lyon1.fr

Table 1. Properties of *LOFAR* and *Very Large Array* data.

Telescope	ν_c (MHz)	σ (mJy beam^{-1})	Resolution (arcsec × arcsec)	σ'^a (mJy beam^{-1})
LOFAR	144	0.22	16.90 × 10.60	0.47
Very Large Array	1400	0.045	16.75 × 14.46	0.050
	4860	0.028	15.63 × 13.50	0.038

[a]The measurements of rms from new images after imaging with new parameters (see details in Section 3.2.2) and smoothing with a 20 arcsec × 20 arcsec Gaussian beam.

2 OBSERVATIONS AND DATA REDUCTION

All data were retrieved from public data archives to study the X-ray emission, radio continuum emission, and molecular gas of the spiral galaxy HCG 97b.

2.1 Chandra observations

Chandra data analysed in this work were obtained using the S3 chip of the Advanced CCD Imaging Spectrometer (ACIS) in the VFAINT mode on 2005 January 14 (ObsID 4988; 57.4 ks). We followed the standard procedure suggested by the Chandra X-ray Center by using the Chandra Interactive Analysis of Observations (CIAO) v4.15.1 and Chandra Calibration Database (CALDB) v4.10.2 to carry out data reduction. The detailed data reduction and analysis descriptions are provided in Hu et al. (2021). In this work, the spectra were extracted using the CIAO tool `specextract` and fitted using XSPEC v12.13.0 and ATOMDB v3.0.9.

2.2 *LOFAR* observations

HCG 97 is within the field-of-view of three pointings (with identifiers of P354+01, P357+01, and ZwCL2341.1 + 0000) from the LoTSS (Shimwell et al. 2017), a deep survey with a typical sensitivity of 0.1 mJy beam^{-1} at good elevations and a resolution of 6 arcsec at the central frequency of 144 MHz. In all three 8-h duration pointings, the target HCG 97 is significantly offset from the pointing centre (>1 deg). To combine the data and improve upon the standard pipeline-processed image quality, we extracted and re-calibrated the *LOFAR* data following the procedure outlined in van Weeren et al. (2021). To do this we first defined a target region with a radius of ∼0.6 deg to include both HCG 97 and enough bright sources for successful re-calibration. Then, sources outside of this region were removed using the full direction-dependent calibration solutions (using kMs and DDFacet; Tasse 2014; Tasse et al. 2018) before the phase centres of visibilities were shifted to the centre of the target region. Before combining the three sets of visibility data, we carried out a beam response correction and updated the visibility weights accordingly. Finally, the re-calibrated step was performed with three rounds of 'tecandphase' calibration and gain calibration using the Default Pre-Processing Pipeline (`DPPP`; van Diepen, Dijkema & Offringa 2018). The final image was produced with `WSClean` (Offringa et al. 2014) with a Briggs robust (Briggs 1995) parameter of 0.0. The rms of the final image is 0.22 mJy beam^{-1} with a beam size of 16.90 arcsec × 10.60 arcsec (see Table 1). Due to projection effects and the low declination of our target, the sensitivity is lower than is achieved for higher elevation LoTSS fields but is consistent with other low declination *LOFAR* studies (e.g. Hale et al. 2019).

2.3 *VLA* observations

Radio continuum data of the galaxy group HCG 97 at GHz frequencies were retrieved from the Very Large Array (*VLA*) archives.

Two *VLA* observations were taken on 2006 November 13 and 2007 April 7 (Project ID: AY171) in the C- and D-configuration with central frequencies of 1.4 GHz and 4.86 GHz, respectively. The total observation time for each configuration is around 2.35 h. The pre-upgrade *VLA* data were analysed and calibrated by using the Common Astronomy Software Applications (CASA) package (McMullin et al. 2007) basically following the official 'Jupiter continuum calibration tutorial'[2] provided by NRAO. In brief, we applied the automatic flagging algorithm `tfcrop` to identify and remove the radio frequency interference, and used 0137+331 (3C48) as the flux calibrator and 0059 + 001 as the phase calibrator to determine the gain solutions for the target (see Grossová et al. 2022 for more detail). Subsequently, further flagging and calibration steps were applied to enhance the quality of the images. After an initial imaging, at least one round of self-calibration was executed to refine the calibration. We used the CASA task `tclean` with the gridding algorithm `wproject` and `multiscale` clean techniques to address widefield non-coplanar baseline effect and ensure proper imaging of the extended radio emission. The target was finally imaged with a Briggs robust 0.0 weighting after the primary-beam correction. The resulting images reach an rms noise of 0.045 mJy beam^{-1} and 0.028 μJy beam^{-1} and the synthesized beam sizes of 16.75 arcsec × 14.46 arcsec and 15.63 arcsec × 13.50 arcsec at 1.4 GHz and 4.86 GHz (see Table 1), respectively.

2.4 ALMA observations

The molecular disc traced by the CO (2-1) line transition of the spiral galaxy HCG 97b was observed by the 12-m Atacama Large Millimeter/submillimeter Array (ALMA) and 7-m Atacama Compact Array (ACA; Project ID: 2018.1.00657.S). Using the Band 6 receiver, a spectral window centred around the CO (2-1) line at 225.262 GHz. The data were calibrated using the ALMA calibration pipeline (version 42030M) in CASA (version 5.4.0–68) and then imaged with the Briggs weighting (robust = 0.5) to balance the sensitivity and resolution. The spectral resolution is 8 MHz, corresponding to 10 km s^{-1}. The resulting synthesized beams in 12-m ALMA and 7-m ACA image data cubes are 0.53 arcsec × 0.42 arcsec and 7.73 arcsec × 4.36 arcsec, respectively. Correspondingly, the achieved rms noises for these data cubes are 3 mJy beam^{-1} and 9 mJy beam^{-1}, respectively.

3 RESULTS

3.1 X-ray properties of two X-ray sources in HCG 97b

The exposure-corrected 0.5–7 keV Chandra ACIS image and DECaLS (Dey et al. 2019) g-band optical image of HCG 97 are presented in Fig. 1, as well as the zoom-in images of the spiral galaxy HCG 97b. X-ray emission of the group shows a clear X-ray plume extending south-east from the group centre, indicating a disturbed galaxy group. At the location of the spiral galaxy HCG 97b, there are two X-ray sources (X1 and X2). These two X-ray sources were also identified by `wavdetect` with the `scale` parameters of 1.0, 2.0, 4.0, 8.0, 16.0, and the significance threshold (`sigthresh`) of 10^6. The X2 is point-like whilst X1 has an elongated shape with major- and minor-axis diameters of ∼7.0 and 3.6 arcsec, respectively. Neither X1 nor X2 is the central AGN as they are off-nuclear and have projected separations of ∼0.86 kpc (∼1.9 arcsec) and ∼5.2 kpc (∼11.6 arcsec), respectively, from the optical centre of the galaxy (marked as a red diamond in Fig. 1).

In order to investigate the nature of these two X-ray sources, we extracted the spectra from circular regions (s1 and s2; see Fig. 2) with radii of 6 and 5 arcsec for sources X1 and X2, respectively. Concerning the possible contamination from group emission, the background spectrum was extracted from an annular region spanning from 15 to 45 arcsec (bkg; see Fig. 2) and encircling two point sources. To model the spectra of two X-ray sources, we used an absorbed power-law model (`phabs*phabs*powerlaw`): the first absorption component was set equal to the line-of-sight Galactic absorption $N_{\rm H} = 3.4 \times 10^{20}\,{\rm cm}^{-2}$ (HI4PI Collaboration 2016), while the other one was set to be free to account for the possible intrinsic absorption of the source. The spectra were fitted and analysed using the Bayesian X-ray Analysis (BXA; Buchner et al. 2014) software and C-statistic to acquire well-defined parameter constraints for spectra with a low number of counts.

For the source X1, the best-fitting photon index is $\Gamma = 2.65 \pm 0.87$ and the absorption column density is $N_{\rm H} = 0.42 \pm 0.26 \times 10^{22}\,{\rm cm}^{-2}$. While for source X2, because of the low number of counts in the region s2, the parameter of the photon index cannot be well constrained. Therefore, we fixed the photon index at 1.6[3] and obtained $N_{\rm H} = 2.28 \pm 0.57 \times 10^{22}\,{\rm cm}^{-2}$, indicating a mildly obscured source. This is consistent with source X2 being surrounded by molecular gas that can be seen in the CO distributions (see Section 3.3). The absorbed 2–10 keV X-ray luminosities of X1 and X2 are $L_{\rm X1,\ 2-10\ keV} = 3.78 \times 10^{39}$ erg s^{-1} and $L_{\rm X2,\ 2-10\ keV} = 1.80 \times 10^{40}$ erg s^{-1}, respectively. The derived X-ray luminosities indicate that the off-centre X-ray sources X1 and X2 could be ULXs ($L_{\rm X} > 10^{39}$ erg s^{-1}; Kaaret, Feng & Roberts 2017). Wang et al. (2016) supports this classification as these two sources (names IC5359-X1 and IC5359-X2) were listed as ULXs in their X-ray point source catalogue.

Near X1, we notice a faint, small-scale X-ray excess, which could be a potential X-ray source (X3; see Fig. 1), although the `wavdetect` failed to identify it. Furthermore, the spectrum of this faint X-ray substructure could not be constrained due to the low-counts limitation. Since the X-ray sources X1 and putative-X3 reside in projection on either side of the optical galaxy centre (see the red diamond in Fig. 1), it is possible that these are fingerprints of two star-forming regions at the two sides of the galactic bar or along it. X3 is fainter than X1, which might be because of an apparent dust lane covering X3, while X1 is not obscured by the dust (see composite DECaLS image in Fig. 3). It is also possible that sources X1 and X3 correspond to jets, but we have not yet been able to assess this with radio data at sufficient angular resolution. Future deeper X-ray data and high-resolution radio studies are needed to assess these scenarios.

3.2 Radio properties of the spiral galaxy HCG 97b

3.2.1 Radio image

The radio images of HCG 97b derived from *LOFAR* 144 MHz, *VLA* 1.4 GHz and 4.86 GHz are presented in Fig. 4 along with the optical image. All radio images reveal an asymmetric morphology, characterized by the radio luminous region located at the disc, along with distinct extraplanar radio emission. In the *VLA* 1.4 GHz and

[2] https://casaguides.nrao.edu/index.php/Jupiter:_continuum_polarization_calibration

[3] We have tested different indices, i.e. from 1.5 to 2.0, the variation in the $N_{\rm H}$ was within 20 per cent, which still suggests source X2 is an obscured source.

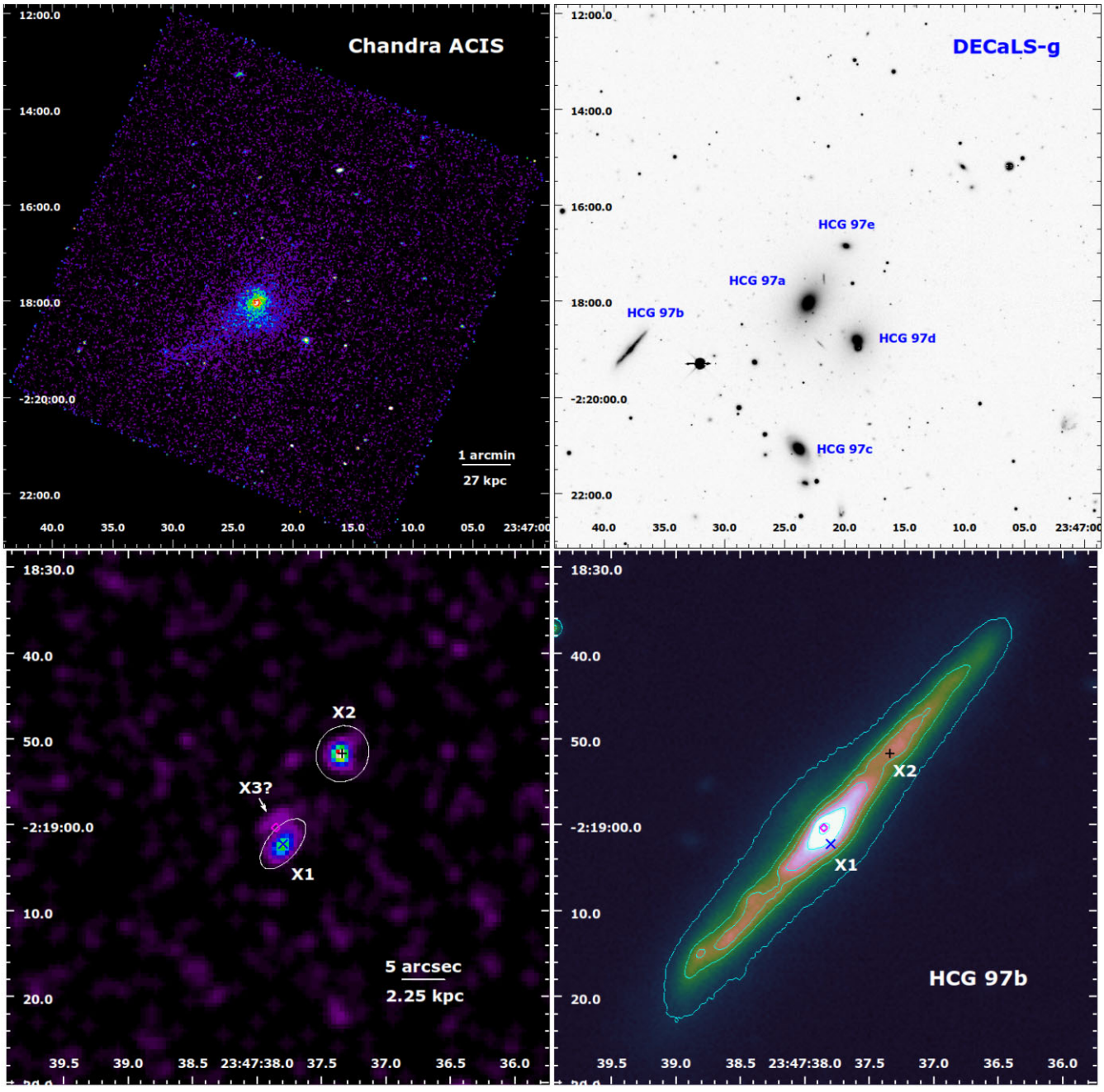

Figure 1. Top: Exposure-corrected 0.5–7 keV Chandra ACIS image of HCG 97 (left) and the DECalS g-band optical image (right). Five member galaxies of HCG 97 are marked. Bottom: Zoom-in view of HCG 97b on the Chandra image (left) and DECalS g-band image with optical contours (right). `wavdetect` regions are presented with two ellipses. For source X1, the major- and minor-axis diameters are ∼7.0 and 3.6 arcsec, respectively; for X2, the major- and minor-axis diameters are ∼6.6 and 6.0 arcsec, respectively. X-ray sources X1 and X2 are marked with a cross and plus sign, respectively. The optical centre is marked with a diamond. The label X3 indicates an extended X-ray source candidate potentially related to the source X1.

4.86 GHz images, the radio emission is curved in the north-west region of the disc, roughly corresponding to the position of X2, and extends ∼27 kpc (∼1 arcmin) in projection outside the disc toward the north-west. We refer to this emission as a radio tail hereafter. This radio tail was visible in Bharadwaj et al. (2014), who used 1.4 GHz NRAO *VLA* Sky Survey (NVSS) radio contours, but this was not the focus of their study. Interestingly, we find two bright radio blobs, one above the disc, and another one outside the disc but near the position of X2 in the *VLA* 4.86 GHz image, potentially indicating a pair of lobes related to the ULX X2. The morphology of the radio tail is not straight and shows evidence of distortion. This might indicate a possible interaction between the radio tail and the IGrM.

The radio tail is also obvious at 144 MHz and is more extended than at GHz frequencies. At the western end of the radio tail, there is a strip of radio emission detected above 3σ in the *LOFAR* 144 MHz image that is possibly an outer part of the radio tail of HCG 97b (we refer to it as an extended tail hereafter), resulting in a total length of ∼60 kpc at low frequency. Interestingly, as presented in Fig. 5, $>5\sigma$ contours on the *LOFAR* 144 MHz image show that there is a decline in brightness in the region between the radio tail

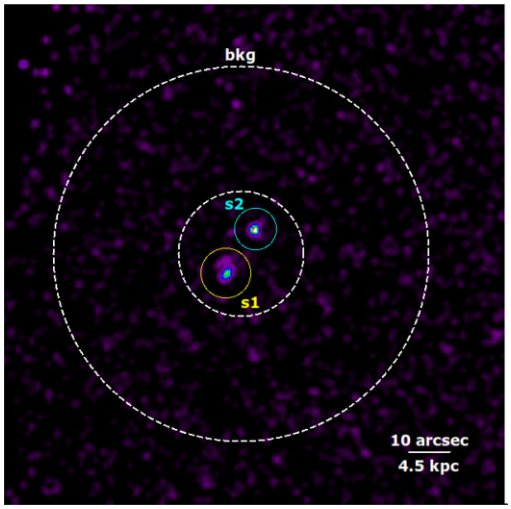

Figure 2. Regions used to extract spectra are presented in the zoom-in Chandra image.

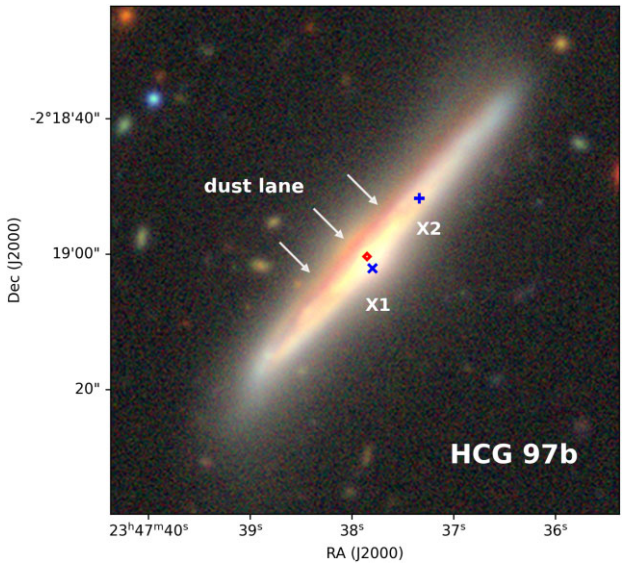

Figure 3. Composite DECalS optical image using g-, r-, and z-band data. X-ray sources X1 and X2 are marked with a cross and plus sign, respectively. The optical centre is marked with a red diamond. The dust lane is also labelled.

and the extended tail. Furthermore, the location of the extended tail coincides with the end part of the X-ray plume from the group centre (or X-ray halo of HCG 97a; also see Fig. 5). This suggests the possibility of an interaction between the extended tail and the IGrM within the X-ray plume, which may lead to the re-ignition of aged radio plasma in the region of the extended tail, possibly due to turbulence or compression. Additionally, we have identified two regions of diffuse radio emission with relatively low significance, situated to the south-west of HCG 97b (see Fig. 4). These regions could potentially represent a second radio tail linked to HCG 97b since there is a lack of clear optical counterparts corresponding to this radio emission, particularly for those regions where the emission exceeds an rms level of $>5\sigma$. To substantiate this observation, it is essential to acquire more extensive and comprehensive radio data, as well as other wavelength data (e.g. Hα data).

3.2.2 *Radio spectrum*

To assess the radio spectrum of HCG 97b, we re-imaged *LOFAR* and *VLA* data with the same lower UV-cut (250λ), Briggs weighting (-0.7), and outer UV-taper (10 arcsec). The resulting images were also convolved to the same resolution (20 arcsec $\times$ 20 arcsec) and re-grided to have the same pixel scale (see Fig. 6). The measurements of rms (σ') from these images are presented in Table 1.

To measure the integrated flux density of radio emission within the disc, tail, and extended tail at three frequency bands, we selected three regions, which are presented in Fig. 7. These regions were set to cover the entire disc and tail with emissions above $5\sigma'$ in each *LOFAR* and *VLA* image, and the flux densities from *LOFAR* and *VLA* images were measured in each region. The extended tail is not detected at two *VLA* frequencies, but at nearly the position of the extended tail, we notice a bright point source at 4.86 GHz and far fainter at 144 MHz.[4] The error on the flux density (σ_{S_ν}) was estimated taking into account the image noise and calibration uncertainty as follows:

$$\sigma_{S_\nu} = \sqrt{(N_{\rm beam} \times \sigma_{\rm rms}^2) + (f \times S_\nu)^2} \quad (1)$$

where $N_{\rm beam}$ is the number of beams covering the entire region of interest, $\sigma_{\rm rms}$ is the local rms noise of the image, and f is the flux scale uncertainty. Here, we adopted $f = 10$ per cent for *LOFAR* observation (Shimwell et al. 2022) and $f = 5$ per cent for *VLA* observations (Perley & Butler 2017).

In Table 2 and Fig. 8, we present the flux density measurements and the spectra of the radio emission in the disc and tail of HCG 97b, respectively. The radio spectra in the disc can be well described by a simple power-law model, revealing a spectral index of -0.83 ± 0.04. While the radio spectra in the tail exhibit a curvature, which is better characterized by an exponential cut-off model described by the equation

$$S(\nu) \propto \nu^{\alpha} e^{-\frac{\nu}{\nu_{\rm b}}} \quad (2)$$

where α is the injection spectrum, and $\nu_{\rm b}$ is the break frequency. The best-fitting parameters indicate a relatively flat injection spectrum ($\alpha_{\rm tail} = -0.56 \pm 0.09$) within the tail and a break frequency at $\sim$9.48 GHz. The flattening trend in the spectra for both disc and tail is also revealed by the spectral index maps (see Fig. 9). We used smoothed images at 144 MHz, 1.4 GHz, and 4.86 GHz to generate the spectral index maps of radio emission from the disc to tail in two frequency bands, i.e. 144 MHz–1.4 GHz and 1.4 GHz–4.86 GHz. In each image, only radio emission above $3\sigma'$ was used to calculate the spectral index. Due to the 20 arcsec $\times$ 20 arcsec resolution and the galaxy being nearly edge-on, the spectral index distribution within the disc cannot be well-resolved. However, general consistency exists between the spectra ($-0.8 \lesssim \alpha \lesssim -0.4$) in the low-frequency band and the spectra ($-1 \lesssim \alpha \lesssim -0.4$) in the high-frequency band. The spectra along the tail are quite uniform and flat ($\alpha \gtrsim -1$) in both frequency bands, and also comparable to those in the disc. The flatness in the tail is potentially influenced by the bright radio blob

[4]The integrated flux densities of this source (2CXO J234727.3-021917; from NED) are measured as <3.13 mJy, 1.04 ± 0.10 mJy, and 0.97 ± 0.08 mJy at 144 MHz, 1.4 GHz, and 4.86 GHz, respectively. The derived spectral index is -0.11 after fitting the three flux densities with a power-law model, suggesting it could be a blazar with a flat spectrum within the MHz to GHz frequency range (Healey et al. 2007; Massaro et al. 2014; d'Antonio et al. 2019) or a variable source on a time-scale of fewer than the interval between two *VLA* observations, i.e. 5 months.

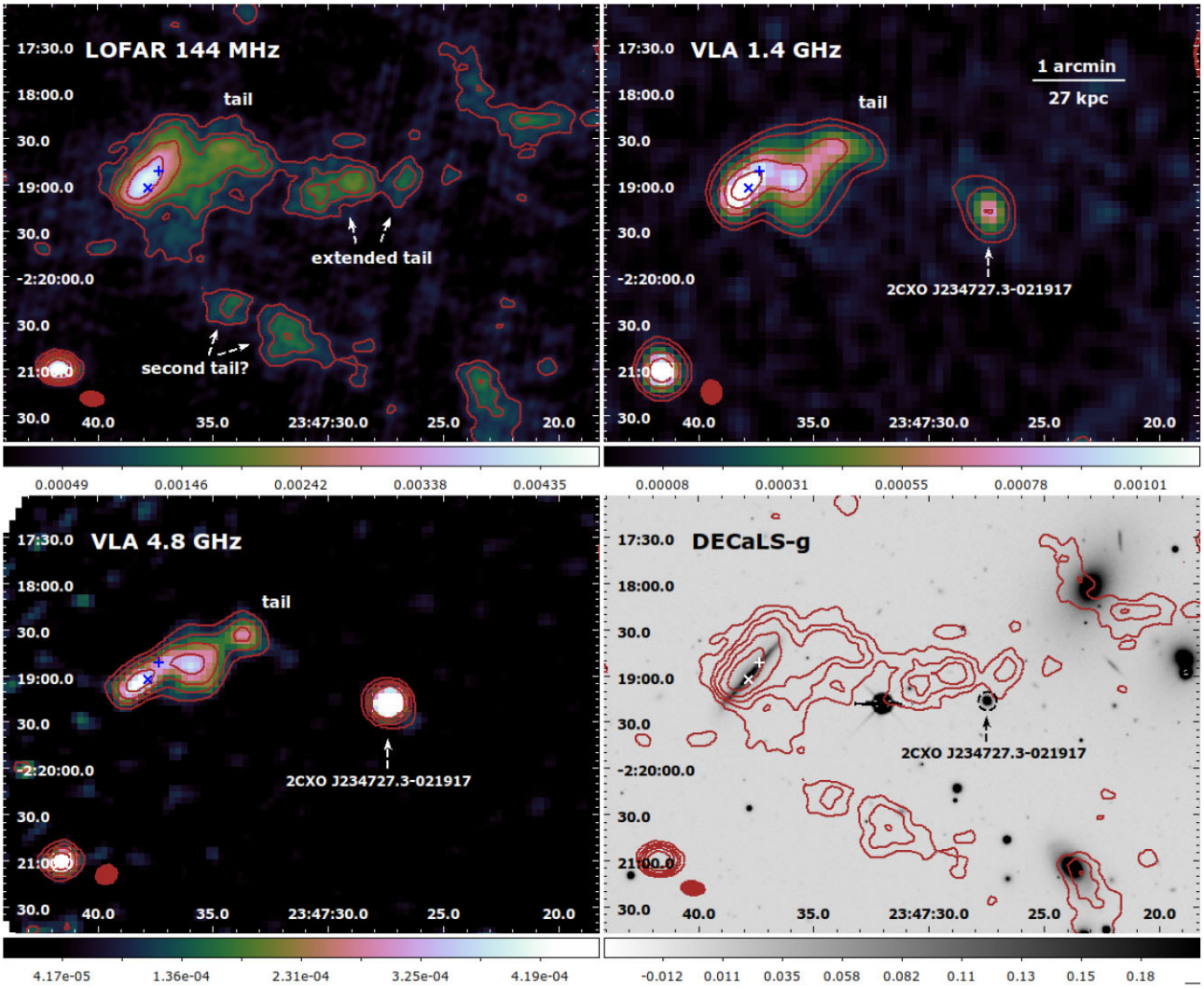

Figure 4. Top-left: *LOFAR* image of HCG 97b at 144 MHZ with a beam size of 16.9 arcsec × 10.60 arcsec. Contours show 3σ, 5σ, 7σ, 10σ, and 15σ flux density levels of radio continuum emission (unit: Jy beam^{-1}). The radio tail, extended tail, and possible southern tail with low significance are all labelled. Top-right: *VLA* image of HCG 97b at 1.4 GHz with a beam size of 16.75 arcsec × 14.46 arcsec. Contours show 3σ, 5σ, 10σ, 15σ, and 20σ flux density levels of radio continuum emission. Bottom left: *VLA* image of HCG 97b at 4.86 GHz with a beam size of 15.63 arcsec × 13.50 arcsec. Contours show 3σ, 5σ, 7σ, and 10σ flux density levels of radio continuum emission. Values in three radio images are in a unit of Jy beam^{-1}. Bottom-right: DECaLS g-band image with 144 MHz contours. Two X-ray sources, X1 and X2, are marked with a cross and plus sign, respectively. A bright point source (2CXO J234727.3-021917) was also labelled.

observed in the tail at 4.86 GHz. We will discuss it in detail in Section 4.2.3.

3.3 CO emission in HCG 97b

3.3.1 CO distribution

The integrated intensity maps of the CO (2-1) emission observed with 12-m ALMA and 7-m ACA are presented in Fig. 10. These maps were generated using a signal masking tool `maskmoment`.[5] The mask, within which moment maps are generated, is defined based on a contour with a high significance level of 5σ. This contour is then expanded to include a surrounding lower-significance contour of 3σ, and is required to cover at least two channels at all pixels.

[5]https://github.com/tonywong94/maskmoment

The CO emission only appears in the disc region and is not detected in the radio tail region. In both the 12-m and 7-m integrated CO intensity maps, the CO emission displays asymmetric morphology. Specifically, the CO (2-1) emission on the south-eastern side of the disc is more intense compared to its counterpart, with a slight extension ∼1.5 arcsec (∼0.67 kpc) from the optical major axis toward the north-east (we labelled it as an 'upturn' feature in Fig. 10).

To further understand the CO distribution and its relationship with the stellar component, we overlaid the 12-m and 7-m integrated CO intensity contours on the composite DECaLS image, as shown in Fig. 11. The optical image with high-resolution 12-m ALMA contours reveals that the central CO emission exhibits an elliptical molecular gas distribution, consistent with the minor inclination of the stellar disc. Notably, on the south-east side of the disc, the distribution of the molecular gas in the 'upturn' feature is closely aligned with both the dust and the blue stellar components, which

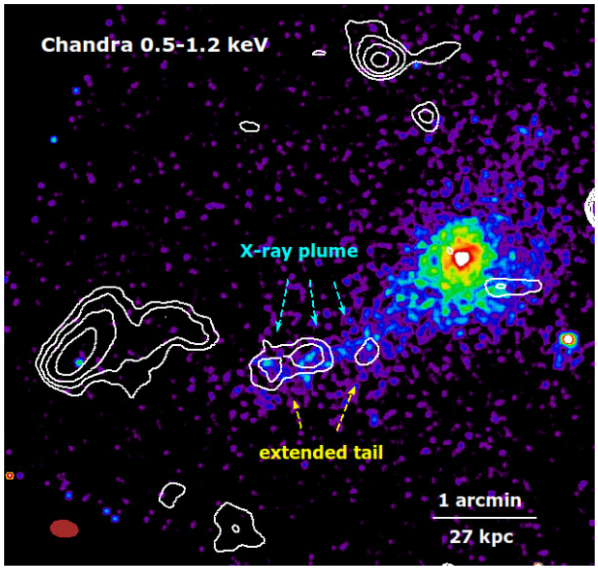

Figure 5. Exposure-corrected 0.5–1.2 keV Chandra ACIS image of HCG 97 with *LOFAR* 144 MHz contours starting from 5σ.

show a gentle bent toward the south-west. However, the optical bent is absent on the north-west side of the stellar disc.

3.3.2 CO kinematics

The intensity-weighted velocity and dispersion maps derived from the 7-m data are also presented in Fig. 10. These maps reveal a maximum and the minimum velocity for the molecular gas of 6877.8 km s^{-1} and 6440.9 km s^{-1}, respectively, yielding an overall velocity differential of approximately 437 km s^{-1}. This suggests that molecular gas follows the galactic disc rotation at an approximate speed of 218 km s^{-1}. Furthermore, the position–velocity diagram (PVD) along the major axis is presented in Fig. 12. The PVD of HCG 97b shows asymmetric kinematics; while the north-west (right) side appears undisturbed, the south-east (left) side exhibits anomalous behaviour. Specifically, a sudden velocity spike occurs at r = 18 arcsec (∼8 kpc) following a plateau in the rotation curve between r = 10 arcsec − 18 arcsec. To highlight this asymmetry, we overlay the contours from the right side of the galaxy onto the left side, suggesting the presence of a recent perturbation in the outer south-east region of the disc. This pattern resembles the observation in the ram-pressure stripped galaxy NGC 4402 (Cramer et al. 2020).

3.4 Molecular gas mass estimation

The total molecular gas mass can be estimated by using $M_{\rm H_2} = \alpha_{\rm CO} L'_{\rm CO}$, and the CO line luminosity can be calculated following the equation (Solomon & Vanden Bout 2005):

$$L'_{\rm CO} = 3.25 \times 10^7 \, S_{\rm CO}\Delta\upsilon \nu_{\rm obs}^{-2} D_{\rm L}^2 \, (1+z)^{-3} \quad (3)$$

where $S_{\rm CO}\Delta\upsilon$ is the CO velocity integrated line flux in Jy km s^{-1}, $\nu_{\rm obs}$ is the observing frequency in GHz, and $D_{\rm L}$ is the luminosity distance in Mpc. Here, we adopted an average CO (2–1)/CO (1–0) line ratio (R21) of 0.64 (den Brok et al. 2021) and a CO(1–0)-to-H_2 conversion factor of $\alpha_{\rm CO} = 4.4\,{\rm M}_\odot$ pc^{-2} (K km s^{-1})$^{-1}$ after correcting the contribution of helium with a factor of 1.36 (den Brok et al. 2023). Therefore, the derived CO (2-1) luminosity of HCG 97b is about 3.6×10^8 K km s^{-1} pc^2 and the total molecular gas mass $M_{\rm H_2}$ is $\sim 2.47 \times 10^9\,{\rm M}_\odot$.

To exhaust all the molecular gas in HCG 97b at the star formation rate of about 1.19 M$_\odot$ yr^{-1} estimated by using the far-infrared luminosity ($L_{\rm FIR} = 3.39 \times 10^9\,{\rm L}_\odot$; obtained from Martinez-Badenes et al. 2012), the gas depletion time $\tau_{\rm dep}$ is estimated to be around $\sim 2.1 \times 10^9$ yr. This is consistent with the average molecular gas depletion time for the discs of normal spiral galaxies ($\sim 2 \times 10^9$ yr; e.g. Bigiel et al. 2008; Leroy et al. 2013), suggesting that the current star formation behaviour in HGC 97b is relatively normal.

4 DISCUSSION

We report the detection of extended radio emission from the spiral galaxy HCG 97b. The *LOFAR* and *VLA* continuum images show elongated emission along the plane of the disc and extended toward the north-west with a ∼27 kpc radio tail. The radio tail extends to ∼60 kpc in the *LOFAR* 144 MHz image, and the outer part of it, i.e. the extended tail (marked in Fig. 4), is potentially associated with the X-ray plume from the group centre (or HCG 97a). The two off-nuclear X-ray sources detected in the spiral galaxy with 2–10 keV luminosity $\sim 10^{39} - 10^{40}$ erg s^{-1} have properties that are consistent with ULXs. The source X2 is mildly obscured ($N_{\rm H} = 2.28 \pm 0.57 \times 10^{22}$ cm^{-2}), which is consistent with its location within the north-western CO emission peak. Moreover, the CO emission in the galaxy displays asymmetric morphology, with the south-eastern side showing greater intensity and alignment with dust and blue stellar components. The PVD reveals asymmetric kinematics, with a sudden velocity spike in the south-east, likely indicative of a recent disturbance such as ram-pressure stripping (e.g. Lee et al. 2017; Cramer et al. 2020; Sardaneta et al. 2022; Roberts et al. 2022b; Cramer et al. 2023).

4.1 Mass estimation of the black holes

ULXs are generally considered the most likely candidates for IMBHs. The black hole mass could be estimated based on the assumption of the Eddington ratio ($\lambda_{\rm Edd} = L_{\rm bol}/L_{\rm Edd}$), and is given by

$$M_{\rm BH} \sim \frac{\kappa_{\rm bol} L_{\rm X} \sigma_{\rm T}}{4\pi G \lambda_{\rm Edd} m_{\rm p} c} \sim 7.96 \times 10^4 \left(\frac{\kappa_{\rm bol}}{10}\right) \times \left(\frac{L_{\rm X}}{1.0 \times 10^{40}\,{\rm erg\,s^{-1}}}\right) \left(\frac{\lambda_{\rm Edd}}{10^{-2}}\right)^{-1} {\rm M}_\odot \quad (4)$$

where $\kappa_{\rm bol}$ is the bolometric correction and $L_{\rm X}$ is the 2–10 keV X-ray luminosity. Here, we scaled $\kappa_{\rm bol}$, $L_{\rm X}$, and $\lambda_{\rm Edd}$ to their typical values. Below, we consider two basic modes of accretion – radiatively inefficient with $\lambda_{\rm Edd} \leq 10^{-2}$ and the standard-disc accretion with $\lambda_{\rm Edd} \sim 1$. These two accretion modes then determine different ranges for the bolometric-correction factor as a function of $L_{\rm X}$.

Assuming a radiatively inefficient mode, we used the luminosity-dependent bolometric correction given by $\kappa_{\rm bol} \approx 13 \times (L_{\rm X}/10^{41}$ erg s$^{-1})^{-0.37}$, which is derived for low-luminosity advection-dominated accretion flow (ADAF) mode of accretion for LLAGNs (Nemmen, Storchi-Bergmann & Eracleous 2014). For the sources X1 and X2, the resulting X-ray bolometric correction factors ($\kappa_{\rm bol}$) are 43.7 and 24.5, and the corresponding bolometric luminosities ($L_{\rm bol}$) are 1.65×10^{41} ergs^{-1} and 4.41×10^{41} ergs^{-1}, respectively. For the ADAF model of accretion, the Eddington ratio is required to be small enough $\lambda_{\rm Edd} \leq 10^{-2}$. If we adopt the upper limit of the Eddington ratio $\lambda_{\rm Edd}$ ($\sim 10^{-2}$), the lower limits of black hole masses for sources X1 and X2 can be obtained as $1.3 \times 10^5\,{\rm M}_\odot$

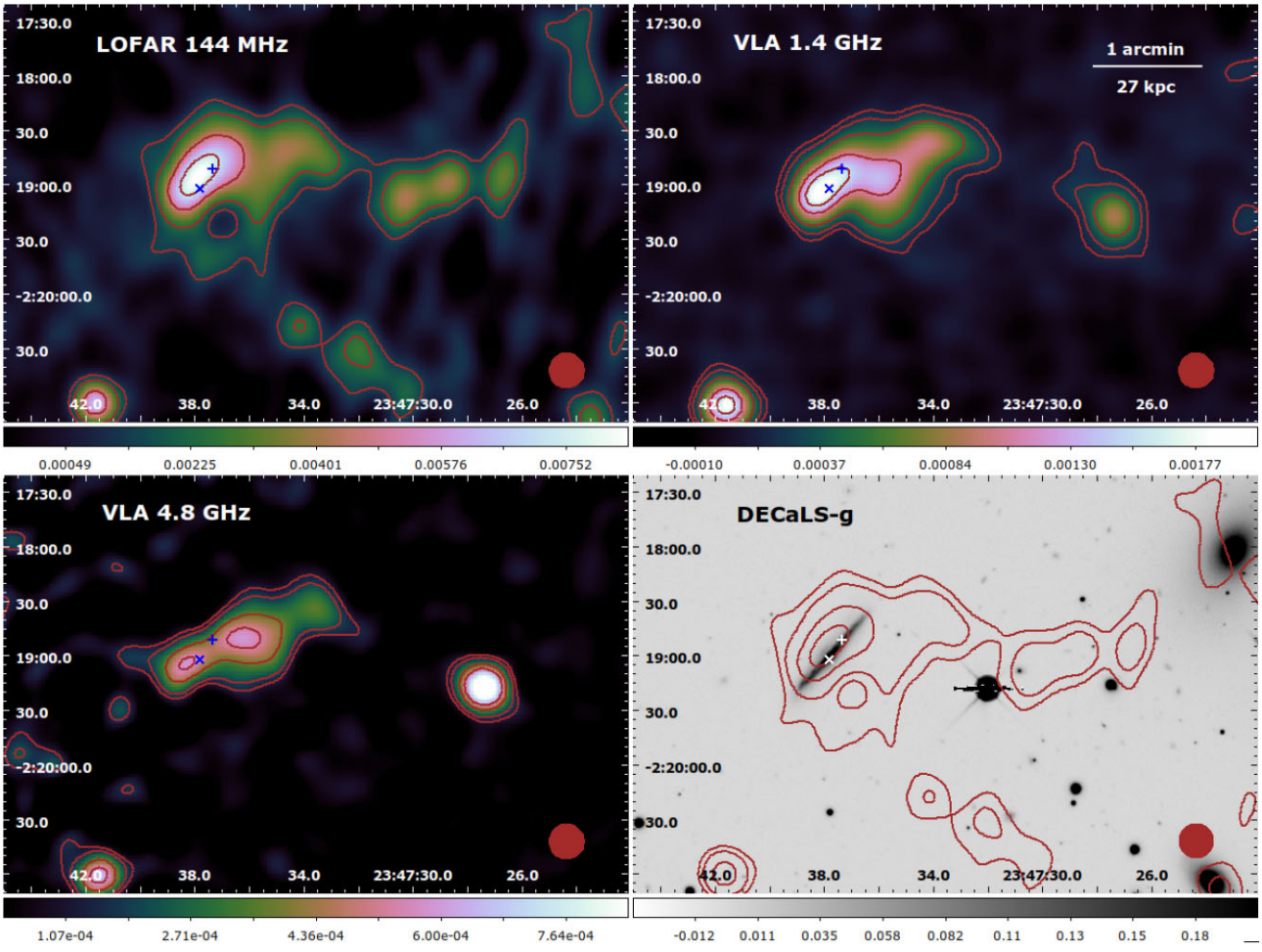

Figure 6. Same as Fig. 4, but all radio images were imaged with new parameters (see details in Section 3.2.2) and smoothed with a 20 arcsec × 20 arcsec Gaussian beam. Contours show $3\sigma'$, $5\sigma'$, $10\sigma'$, $15\sigma'$ and $20\sigma'$ flux density levels of radio continuum emission.

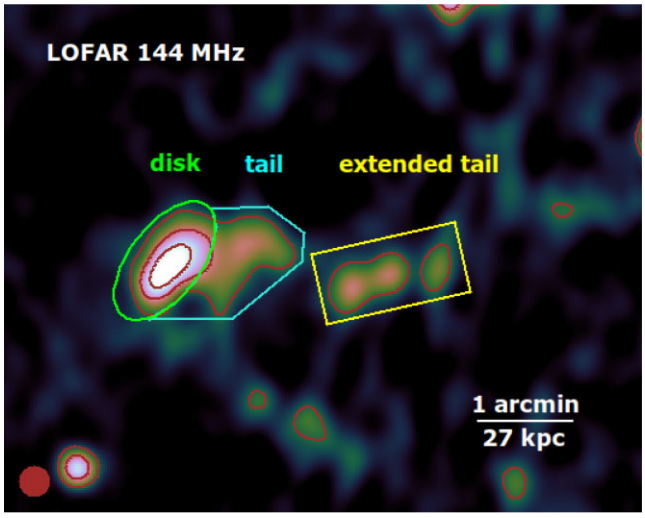

Figure 7. *LOFAR* 144 MHz image with regions selected to measure the integrated flux density. **The ellipse, polygon, and box represent** the disc, tail, and extended tail region, respectively.

and $3.5 \times 10^5\,M_\odot$, respectively. In the radiatively inefficient mode, the Eddington ratio is not expected to be smaller than $\lambda_{\rm Edd} \leq 3.5 \times 10^{-3}$ since then the X2 mass exceeds $10^6\,M_\odot$, which is inconsistent with the absence of the major merger fingerprints. If the accretion proceeds effectively via a standard disc with an Eddington ratio close to the unity ($\lambda_{\rm Edd} \sim 1$), the X1 and X2 masses would be pushed even lower. In this case, we used the bolometric correction $\kappa_{\rm bol} = 7 \times (L_{\rm X}/10^{42}\ {\rm ergs}^{-1})^{0.3}$ for a thin disc following Netzer (2019) and derived the $\kappa_{\rm bol}$ as 1.3 and 2.1 for the X1 and X2 2–10 keV luminosity, respectively. Therefore, the black hole masses are 39.5 $M_\odot$ and 300.4 $M_\odot$ for sources X1 and X2, respectively. This shows that the X2 is consistent with being an IMBH, while X1 could even be a stellar-mass black hole accreting close to or even exceeding an Eddington rate. While if a super-Eddington accretion ($\lambda_{\rm Edd} \approx 10^2$) is assumed, the black hole mass of X1 and X2 are 0.4 $M_\odot$ and 3.0 $M_\odot$, respectively, placing them both within the stellar-mass black hole range. The measurements of black hole masses are also summarised in Table 3.

A further way to ascertain the black hole mass is to use the Fundamental plane correlation between X-ray luminosity and radio luminosity (Merloni, Heinz & di Matteo 2003; Plotkin et al. 2012; Dong, Wu & Cao 2014; Gültekin et al. 2019). Since we detected no compact radio sources spatially co-aligned with X1 and X2, we estimated limits on the integrated radio

Table 2. Properties of radio continuum emission of HCG 97b.

Region	$S_{144\ \mathrm{MHz}}$ (mJy)	$S_{1.4\ \mathrm{GHz}}$ (mJy)	$S_{4.86\ \mathrm{GHz}}$ (mJy)	$\alpha^{1.4\ \mathrm{GHz}}_{144\ \mathrm{MHz}}$	$\alpha^{4.86\ \mathrm{GHz}}_{1.4\ \mathrm{GHz}}$
Disc	26.45 ± 3.02	4.56 ± 0.35	1.41 ± 0.14	-0.77 ± 0.06	-0.94 ± 0.05
Tail	19.63 ± 2.52	4.86 ± 0.38	1.69 ± 0.17	-0.61 ± 0.07	-0.85 ± 0.06
Extended tail	18.09 ± 2.47	–	–	–	–

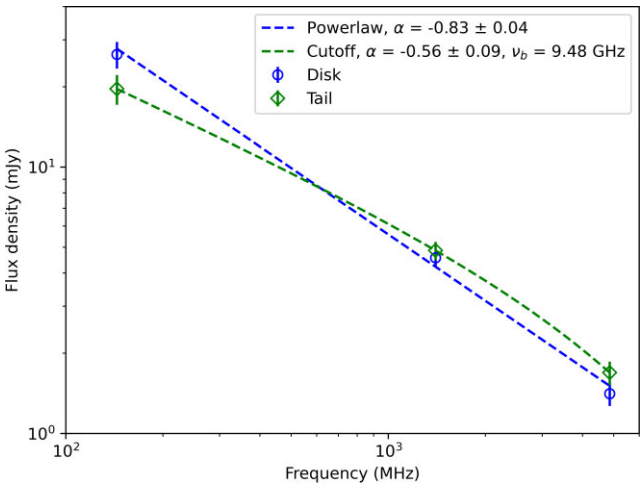

Figure 8. Radio spectra in the disc and tail of HCG 97b at three frequencies. The best fits for the disc and tail are also presented.

luminosities using the same regions as in the X-ray spectral analysis (see Section 3.1). The upper limits of the radio luminosities for X1 and X2 are $L_{\mathrm{X1,\ 4.8\ GHz}} = 4.03 \times 10^{36}$ erg s^{-1} and $L_{\mathrm{X2,\ 4.8\ GHz}} = 3.16 \times 10^{36}$ erg s^{-1}. Following the Fundamental Plane correlations proposed by Gültekin et al. (2019), $\log(M_{\mathrm{BH}}/10^8\ \mathrm{M}_\odot) = (0.55 \pm 0.22) + (1.09 \pm 0.10)\log(L_{\mathrm{R,\ 5.0\ GHz}}/10^{38}\ \mathrm{erg\ s^{-1}}) + (-0.59^{+0.16}_{-0.15})\log(L_{\mathrm{X,\ 2-10\ keV}}/10^{40}\ \mathrm{erg\ s^{-1}})$, the black hole masses are constrained as $\leq (1.9 \pm 1.3) \times 10^7\ \mathrm{M}_\odot$ for X1 and $\leq (5.8 \pm 3.9) \times 10^6\ \mathrm{M}_\odot$ for X2, which also suggests the X2 could fall into the IMBH mass range.

4.2 Ram-pressure stripped radio tail

The observed extended, one-sided asymmetric shape of the radio tail, in conjunction with the asymmetry in CO morphology and kinematics, suggests that the galaxy may be experiencing ram pressure, likely giving rise to the formation of a stripped radio tail.

4.2.1 Ram pressure direction

The stellar disc and molecular gas distributions in HCG 97b (see Figs 11 and 13) exhibit a bent or 'upturn' feature which offsets to the north of the major axis. Correspondingly, in the Galaxy Evolution Explorer (GALEX) near-UV (NUV) image (the bottom panel of Fig. 13), the peak NUV emission coincides with this 'upturn', implying a similar offset distribution for young stars. Given that HCG 97b is not a real edge-on galaxy – with an estimated inclination angle of 85°–88°, this 'upturn' feature is likely not an extraplanar feature but rather indicative of a non-axisymmetric disc feature. These observed features in HCG 97b resemble those in the Virgo cluster galaxy NGC 4654. NGC 4654 has two asymmetric spiral arms, where the shorter arm ends in a bright star-forming region at the outer edge of the gas disc, aligning with the leading side of the ram pressure interaction (Koopmann & Kenney 2004; Chung et al. 2009). The distributions of stars and gas in NGC 4654 are believed to be the result of combined effects, including gravitational interaction (∼500 Myr ago) and ram pressure stripping (ongoing; Vollmer 2003). Therefore, HCG 97b could resemble the NGC 4654 but viewed from a different angle. Moreover, the radio tail of HCG 97b is extended toward the north-west and radio contours on the south-east side are compressed and tight compared with those on the other side (see Fig. 4), suggesting the direction of the ram pressure should be from the south-east (see the indication of the ram pressure direction in Fig. 13).

This scenario is also indicated by the elongated X-ray plume from the central galaxy HCG 97a toward the south-east, presented in Figs 1 and 5. Since the X-ray plume is roughly extended in the direction of HCG 97b, it is likely an X-ray tail stripped from the hot gas halo of HCG 97a or the central IGrM during the past interaction between HCG 97a and HCG 97b. This is also the case for M86, with a possible encounter of NGC 4438 first reported in Kenney et al. (2008), and NGC 4438 shows a clear sign of tidal interaction. However, the disc morphology of HCG 97b is not strongly perturbed, suggesting that the X-ray plume might have been formed in the past by the interaction between HCG 97a and other galaxies. Alternatively, it could also be a scenario that HCG 97b with a sub-group fell into the main group HCG 97 in the past, and the X-ray halo of the sub-group was grabbed by the main group during the first pericentric passage, forming an X-ray plume pointing to the motion direction. We also notice that the extended radio tail detected in the *LOFAR* 144 MHz image coincides with the end of the X-ray plume. This scenario could be that the striped tail of HCG 97b encountered the X-ray plume, and then the low-frequency radio emission was 're-ignited' by the turbulence or compression possibly triggered by the bulk motion in the X-ray plume. Considering a typical radiative time range of CRe at 144 MHz (∼1–2 × 10^8 yr; Basu et al. 2015), the stripped scale of the radio tail could be estimated as ∼36–74 kpc after assuming that the velocity of CRe follows the relative galaxy velocity ($v \approx 360$ km s^{-1}), which is the difference between the velocities of HCG 97b ($cz_{\mathrm{HCG\ 97b}} = 6940$ km s^{-1}; Hickson et al. 1992) and the group mean ($cz_{\mathrm{HCG\ 97}} = 6579$ km s^{-1}; Jones et al. 2023). It suggests that there could exist old radio plasma at the 60 kpc radio tail still emitting radio emission at 144 MHz.

4.2.2 Capabilities of ram-pressure stripping and gravitational interaction

Theoretically, ram-pressure stripping and gravitational or tidal interactions are inevitable phenomena for galaxies orbiting within a galaxy group environment. To quantify these effects for HCG 97b, we conduct approximate calculations to estimate the relative capabilities of the ram-pressure stripping and gravitation interaction.

To derive the distributions of the ram pressure and radial tidal interaction, we first determine the electron number density and total mass of the HCG 97 group by using a revised thermodynamical

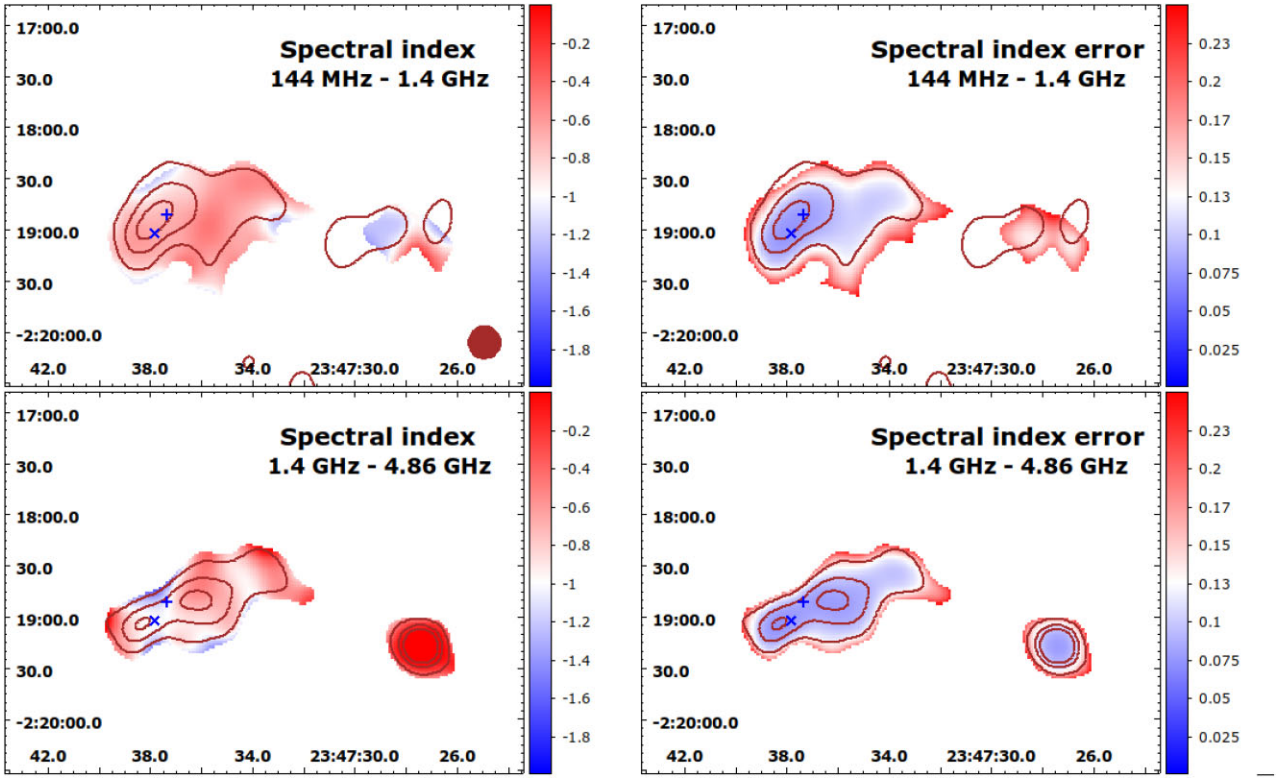

Figure 9. Spectral index (left) and error (right) maps of radio emission of HCG 97b. *LOFAR* 144 MHz contours and *VLA* 1.4 GHz contours derived from the smoothed *LOFAR* image and *VLA* image are overlaid on 144 MHz–1.4 GHz and 1.4 GHz–4.86 GHz plots, respectively. All contours are starting from $5\sigma'$. The beam shape with a size of 20 arcsec × 20 arcsec is also marked at the right-bottom corner with a filled circle.

ICM (RTI) model [see Zhu et al. (2016, 2021) for details of the RTI model], and present the results with 68 per cent confidence level in Fig. 14.

Following the method described in Jáchym et al. (2014), the ram pressure can be estimated as

$$P_{\rm ram} = \rho_{\rm gas,IGrM} \upsilon^2 = \mu_{\rm e} m_{\rm u} n_{\rm e,IGrM} \upsilon^2 \tag{5}$$

where $\rho_{\rm gas,IGrM} = \mu_{\rm e} m_{\rm u} n_{\rm e,IGrM}$ is the gas mass density of the group at the position of the galaxy, $m_{\rm u}$ is the atomic mass unit, and υ is the 3D infalling velocity of HCG 97b. Since the relative galaxy velocity ($\sim$360 km s^{-1}) is lower than the group velocity dispersion ($\sigma_{\rm HCG\ 97} \approx 371.5$ km s^{-1}; Hickson et al. 1992), we adopt the group velocity dispersion here to approximate the 3D infalling velocity υ ($\approx \sqrt{3}\sigma_{\rm HCG\ 97}$). Then, we compare the ram pressure acting on the galaxy's atomic gas with the gravitational restoring force in the galaxy. The latter can be approximated by the centrifugal force at the galaxy's outer radius (R) with an expression of $a = v_{\rm rot}^2/R$, where $v_{\rm rot} = 218$ km s^{-1} is the rotation velocity obtained from the ALMA data (see Section 3.3). Assuming a typical column density ($\Sigma_{\rm HI} \sim 10\ {\rm M}_\odot\ {\rm pc}^{-2}$) of the galaxy's atomic gas and a flat rotation curve, the radius R can be associated with the stripping radius, which can be estimated as

$$R_{\rm strip} = v_{\rm rot}^2 \Sigma_{\rm HI} / P_{\rm ram} \tag{6}$$

The derived ram pressure and stripped radius are present in Fig. 15.

Following the calculations provided by Henriksen & Byrd (1996) and Cortese et al. (2007), we calculate the strength of the galaxy-group gravitational interaction as HCG 97b falling into the group potential well. It can be quantified based on the comparison between the radial tidal acceleration ($a_{\rm rad}$) and internal galaxy acceleration ($a_{\rm gal}$), which are given by

$$a_{\rm rad} = G M_{\rm pert} \left[\frac{1}{r^2} - \frac{1}{(R+r)^2} \right] \tag{7}$$

$$a_{\rm gal} = \frac{G M_{\rm dyn}}{R^2} \tag{8}$$

where $M_{\rm pert}$ is the total mass of the perturber (i.e. galaxy group HCG 97) within r, $M_{\rm dyn}$ is the dynamic mass of the perturbed galaxy (i.e. HCG 97b), R is the radius of the perturbed galaxy, and r is the separation between the perturber and perturbed galaxy. The radial tidal acceleration has the effect of pulling the matter at either side of the disc away from the galaxy and approaching the perturber. We estimate the dynamic mass of HCG 97b ($M_{\rm dyn} \sim 7 \times 10^{11}$ M$_\odot$) based on the stellar mass–halo mass relationship provided by Behroozi, Wechsler & Conroy (2013). If the radial tidal acceleration is stronger than the internal galaxy acceleration, the matter on the infalling galaxy is able to be stripped. The corresponding stripped radius (i.e. truncation radius $R_{\rm trunc}$) can be estimated by

$$R_{\rm trunc} \approx r \left(\frac{M_{\rm dyn}}{M_{\rm pert}(< r)} \right)^{1/3} \tag{9}$$

We present the ratio between two accelerations ($a_{\rm rad}/a_{\rm gal}$) and the truncation radius as a function of the distance r in Fig. 16. These results agree well with the case of the galaxy with a stellar mass of 10^{10} M$_\odot$ within a group environment (see the green solid lines in their figs 7 and 8) provided in Boselli, Fossati & Sun (2022).

From the plots in Figs 15 and 16, it can be observed that if HCG 97b is an infalling galaxy approaching the group centre, neither ram pressure nor tidal interaction would have a significant impact on

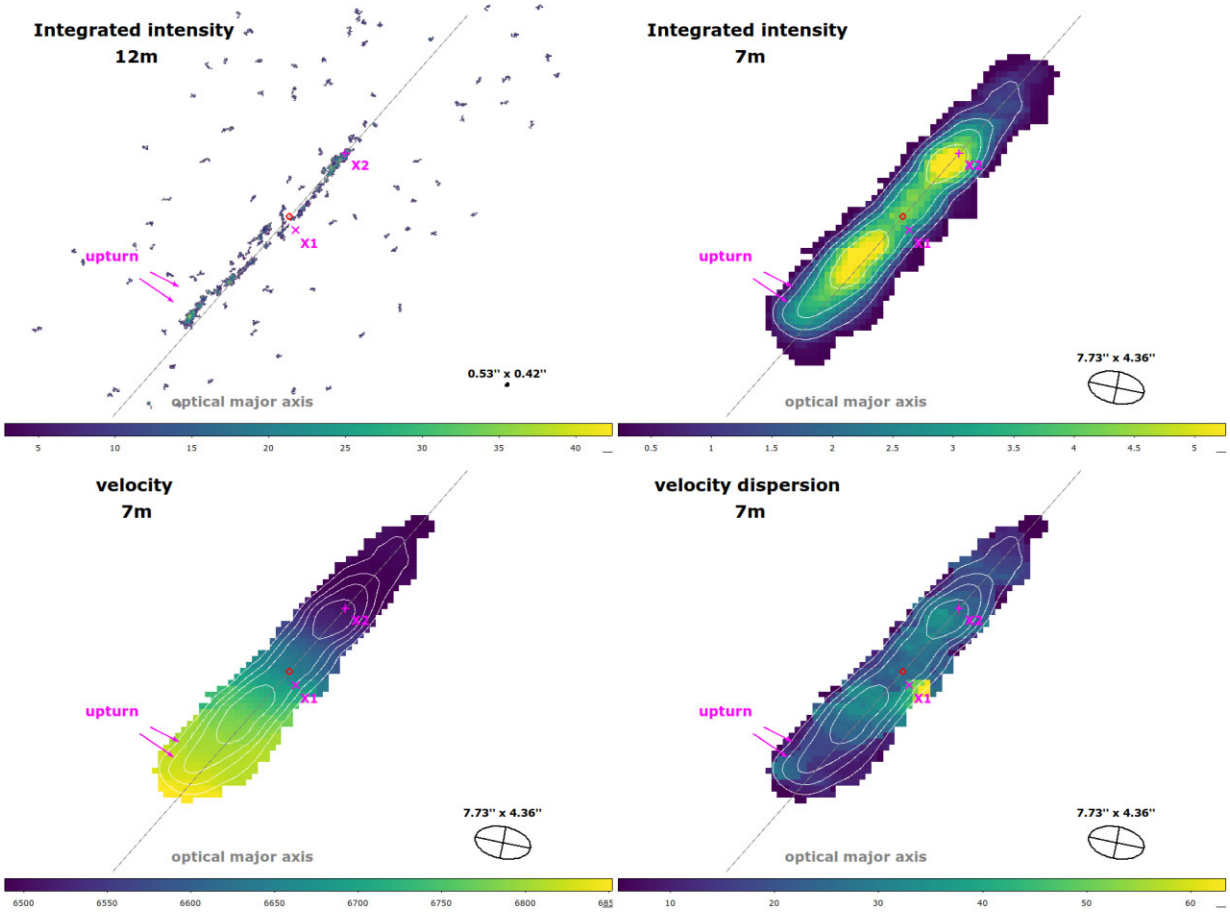

Figure 10. Top: The integrated intensity (unit: K km s^{-1}) map of CO (2-1) line emission observed with 12-m ALMA (left) and 7-m ACA (right). The beam sizes for 12-m and 7-m data are 0.53 arcsec × 0.42 arcsec and 7.73 arcsec × 4.36 arcsec, respectively. Contours are presented with values of (5, 15, 30) K km s^{-1} for 12-m data and (1, 2, 3, 4) K km s^{-1} for 7-m data. Bottom: The intensity-weighted velocity (unit: km s^{-1}) and the corresponding velocity dispersion (unit: km s^{-1}) maps of molecular gas observed with 7-m ACA. The galactic centre and two X-ray sources are marked. The major axis of the optical disc is also overlaid.

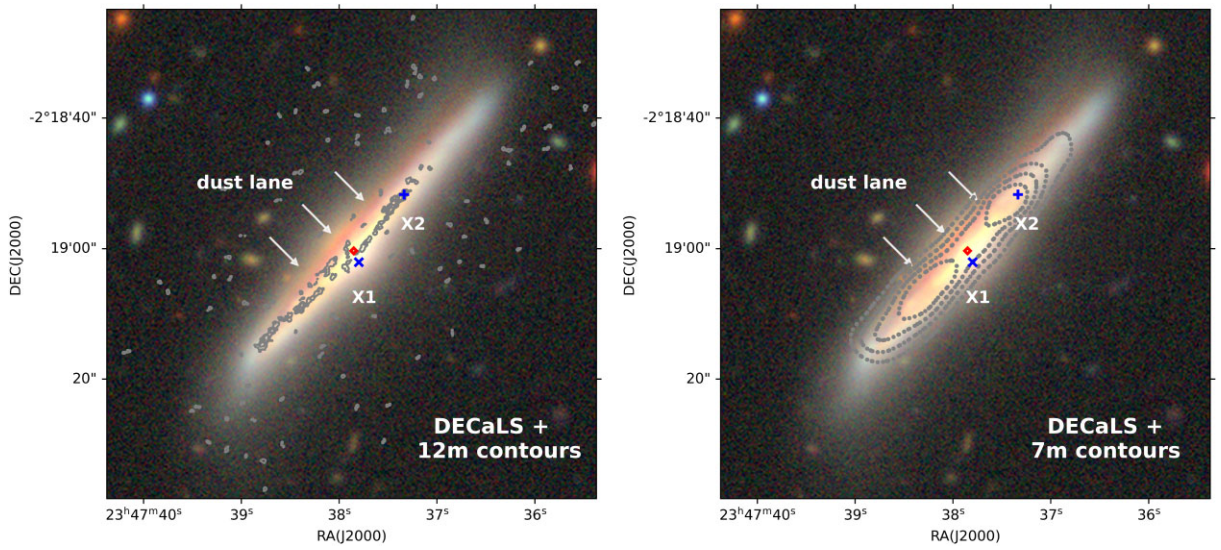

Figure 11. The 12-m (left) and 7-m (right) integrated CO (2-1) intensity contours are overlaid on the composite DECaLS image.

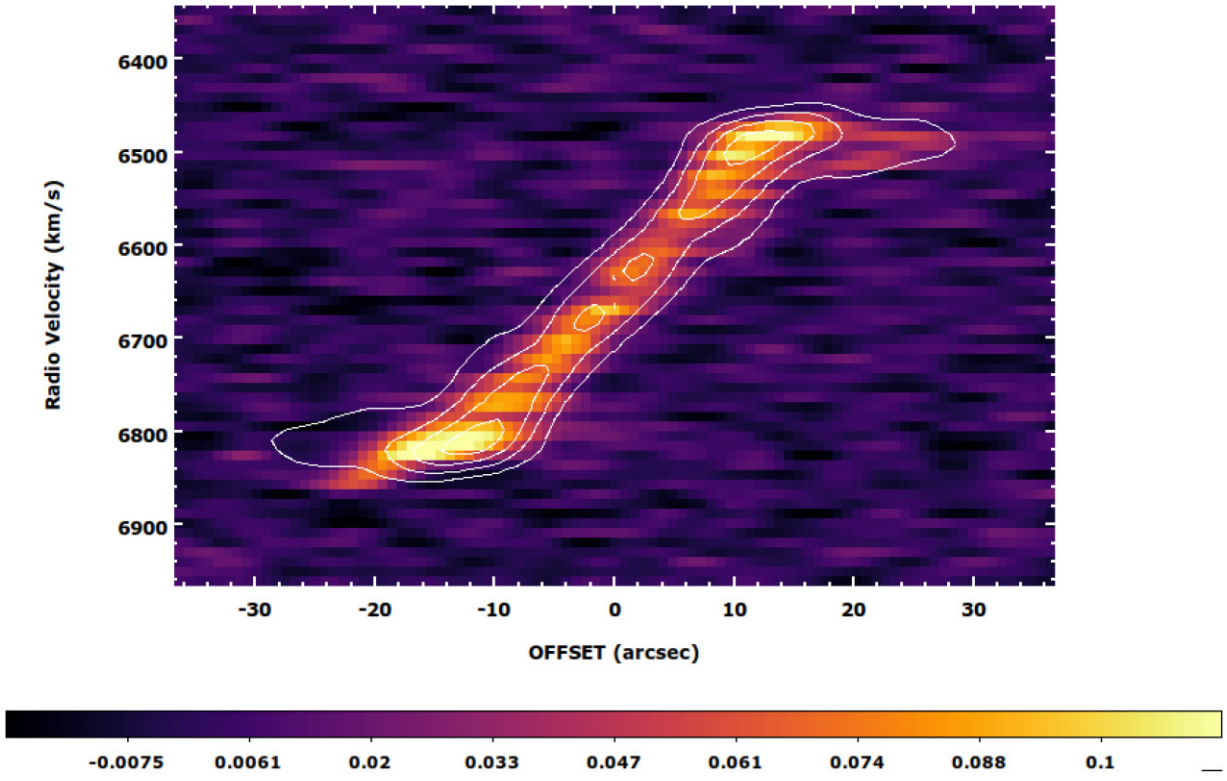

Figure 12. The PVD of 7-m CO (2-1) emission along the major axis of HCG 97b. Contour levels are 0.02, 0.04, 0.06, and 0.08 Jy beam^{-1}. In contours, a mirror of the right (north-west) side of the galaxy is overlaid on the left (south-east) side.

Table 3. Estimations of black hole masses for two ULXs, X1, and X2, for different Eddington ratios and the fundamental plane relation.

	$M_{\rm BH}$ ($M_\odot$)			
X-ray source	$\lambda_{\rm Edd} = 10^2$	$\lambda_{\rm Edd} = 1$	$\lambda_{\rm Edd} = 10^{-2}$	Fundamental plane
X1	0.4	39.5	1.3×10^5	$\leq(1.9 \pm 1.3) \times 10^7$
X2	3.0	300.4	3.5×10^5	$\leq(5.8 \pm 3.9) \times 10^6$
Accretion mode	Slim disc	Slim/standard disc	ADAF	

In the last row, we distinguish different accretion modes for the corresponding Eddington ratios.

HCG 97b, because both the stripped radius and truncation radius are quite larger than the radius of HCG 97b. Therefore, it confirms that HCG 97b has undergone the first pericentric passage and is currently receding from the group centre. Given that the optical disc of HCG 97b does not exhibit obviously disturbed morphology (only a possible weak warp shape), it is plausible to assume that the separation between HCG 97b and the group centre during the first pericentric passage was not extremely close, perhaps greater than the disc radius of HCG 97b ($R_{97b} = 1.23$ arcmin $= 16.2$ kpc). It is more probable that HCG 97b has experienced the closest distance of $\gtrsim$20–30 kpc between the group centre and HCG 97b. At this distance, both hydrodynamic and gravitational processes likely played roles in gas stripping. The gravitational interaction might cause a possible mild warp of the disc and possibly flatten the galaxy's gravitational potential well, enhancing the efficiency of ram pressure. This is supported by the curve in Fig. 16, which suggests a mild gravitational interaction effect with values of $a_{\rm rad}/a_{\rm gal} \sim 10^{-1}$ for $r \approx$ 20–30 kpc. It is also worth noting that the real ram pressure would be even higher because the current relative velocity of HCG 97b has been largely reduced after the first pericentric passage.

More recently, Jones et al. (2023) used *VLA* data to measure the H I emission of Hickson Compact Groups (HCGs) and reported that for the group of HCG 97, the H I emission is only detected in the member galaxy HCG 97b and its morphology is more extended at the northern side of the disc, implying that HCG 97b is likely a new, gas-rich galaxy infalling into an evolved group. They also measured the $M_{\rm HI}$ deficiency Def($M_{\rm HI}$) = 0.79 of HCG 97b, which is the logarithmic difference between the predicted value (log $M_{\rm HI,pred} = 9.47\,{\rm M}_\odot$) and observed one (log $M_{\rm HI} = 8.68\,{\rm M}_\odot$). Martinez-Badenes et al. (2012) also measured Def($M_{\rm HI}$) but inferred a higher value of Def($M_{\rm HI}$) =1.53. The difference between the $M_{\rm HI}$ deficiency in the two papers is probably because Jones et al. (2023) used the improved imaging (e.g. multi-scale clean) and masking (e.g. `SoFiA`) methods to recover as much flux of HCG 97b as possible, thus obtaining a smaller deficient value. Nonetheless, both works suggest that a considerable part of H I was removed from HCG 97b due to the possible interaction between the infalling galaxy

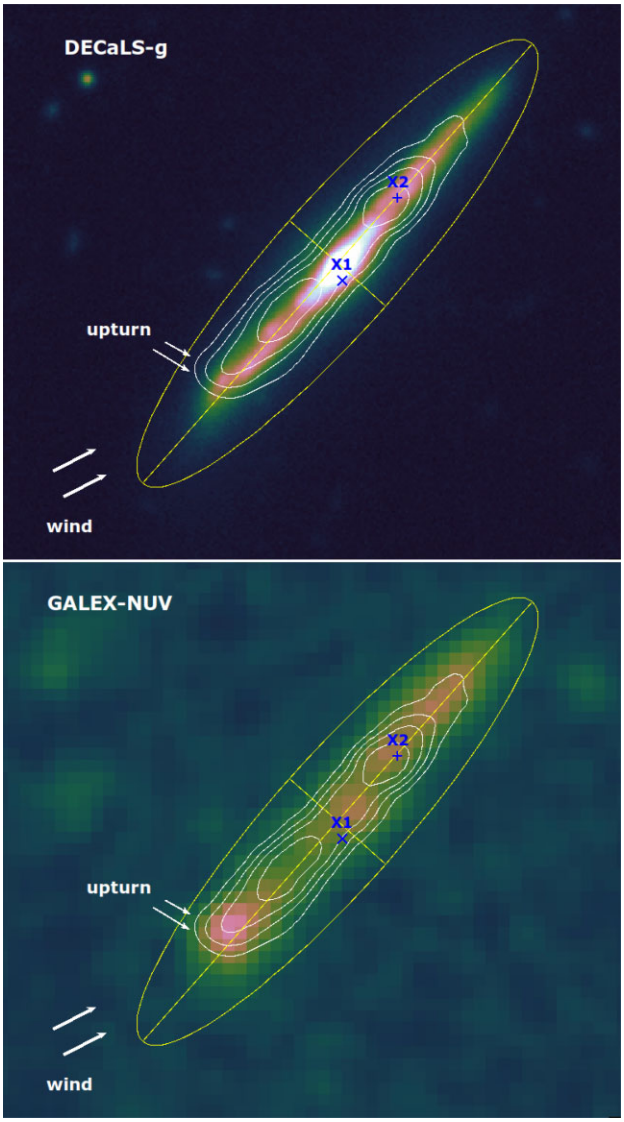

Figure 13. DeCaLS g-band image (top) and GALEX NUV image (bottom) with ALMA integrated intensity contours. The feature 'upturn' and two X-ray sources are marked. The IGrM wind due to the ram pressure is indicated. The major and minor axes of the optical disc are also overlaid.

and IGrM. Furthermore, Rasmussen et al. (2008) modelled ram-pressure stripping in HCG 97b and reported that up to $2 \times 10^9\,M_\odot$ of H I could have been stripped from a galaxy with a stellar mass of $3.2 \times 10^{10}\,M_\odot$. This value is roughly consistent with the observed deficiency of HCG 97b (Jones et al. 2023).

4.2.3 Atypical spectral indices in the radio tail

In the case of HCG 97b, radio spectral indices in the radio tail differ from typical ram-pressure stripped tails, showing flatter values comparable to those in the radio disc, both in the integrated spectra and in the spectral index maps. This contradicts the expected steeper spectral indices ($\alpha < -1$) in stripped tails due to synchrotron radiative cooling (i.e. Vollmer et al. 2004, 2021; Chen et al. 2020; Müller et al. 2021; Ignesti et al. 2022; Roberts et al. 2022a). We note that while non-thermal emission (synchrotron emission) dominates the radio emission at $\nu \lesssim 10$ GHz in most nearby galaxies, thermal emission (free–free emission) could also contribute a fraction of $f_{\rm th} \approx 1$ per cent $-$ 40 per cent of the observed total radio emission (Klein, Lisenfeld & Verley 2018, and the references therein). Since there is a lack of Hα data to estimate the thermal emission for HCG 97b directly, we approximate the non-thermal emission by assuming thermal emission fractions of 2.3 per cent, 8.6 per cent, and 16.6 per cent at 144 MHz, 1.4 GHz, and 4.86 GHz, respectively, based on equation (8) provided by Tabatabaei et al. (2017). We present the estimated non-thermal spectra in the disc and tail, along with the best fits with the exponential cut-off model in Fig. 17. The non-thermal spectra in the disc indicate a more curved shape and an injection spectral index of $\alpha_{\rm nth}^{\rm disk} \approx -0.75 \pm 0.09$. While the new spectra in the tail suggest an unchanged injection spectral index ($\alpha_{\rm nth}^{\rm tail} \approx -0.57 \pm 0.09$), but a lower break frequency. The spectrum break frequency in the tail ($\nu_{\rm c}^{\rm tail} \approx 8.0 \pm 4.0$ GHz) appears to be smaller than the one in the disc ($\nu_{\rm c}^{\rm disk} \approx 10.4 \pm 6.5$ GHz), suggesting a slight difference in a radiative time-scale which can be derived with the expression presented in Miley (1980),

$$t_r \propto 3.2 \times 10^{10} \frac{B^{1/2}}{B^2 + B_{\rm CMB}^2} \frac{1}{\sqrt{\nu_{\rm c}(1+z)}}\ {\rm yr} \quad (10)$$

where $B_{\rm CMB} = 3.25(1+z)^2\,\mu$G is the equivalent cosmic microwave background magnetic field and $\nu_{\rm c}$ is the cut-off frequency in units of MHz. Assuming a typical magnetic field of $\sim$10 μG within the disc and $\sim$5 μG within the tail (Tabatabaei et al. 2017; Müller et al. 2021; Ignesti et al. 2022), the radiative times are estimated at $8.8 \pm 2.7 \times 10^6$ yr and $2.2 \pm 0.5 \times 10^7$ yr for the disc and tail, respectively.

The observed flat spectrum in the tail with its longer radiative time-scale indicates that the CRe within the tail may have undergone rapid displacement or uplift from the disc, to an extent where the typical spectral aging effects are not observed. To quantify this displacement, we adopt a derived age of approximately $2.2 \pm 0.5 \times 10^7$ yr for the CRe in the tail and a projected tail length of approximately 30 kpc. Consequently, we infer an expected velocity for the radio plasma transported from the disc to the tail of roughly 1300 km s^{-1}. This velocity is much higher than the velocity measured in ram-pressure stripped galaxies (100 $-$ 600 km s^{-1}; Ignesti et al. 2023), and aligns more closely with scenarios observed in head-tail galaxies where the plasma is accelerated out of the galaxy by the AGN (e.g. Ignesti et al. 2020; Edler et al. 2022). Given that the injection spectral indices for both disc and tail are consistent with the characteristics of fresh injected plasma typically associated with AGN activity, and taking into account the proximity of the two bright radio blobs detected at 4.86 GHz to the X2 source, we propose that the CRe may have been uplifted through a mechanism involving ULX feedback – potentially linked to IMBH activity, in addition to the conventional ram-pressure stripping process. In the upcoming section (Section 4.3), we will discuss the potential contribution of IMBH activity in more detail. Furthermore, the absence of spectral aging effects outside of the disc could also be attributed to efficient adiabatic expansion losses. The energy loss due to adiabatic expansion is linearly proportional to the CRe energy (E), while losses from synchrotron are proportional to the square of the energy (E^2; Longair 2011). Considering that the thermal pressure in the galaxy group environments should be lower than in the ICM, the adiabatic losses might be more efficient since the ISM can expand more easily.

4.3 Enhanced ram-pressure stripping due to an accreting IMBH?

A peculiarity of the spiral galaxy HCG 97b is the presence of two off-nuclear X-ray sources, with the X2 source being more distant from

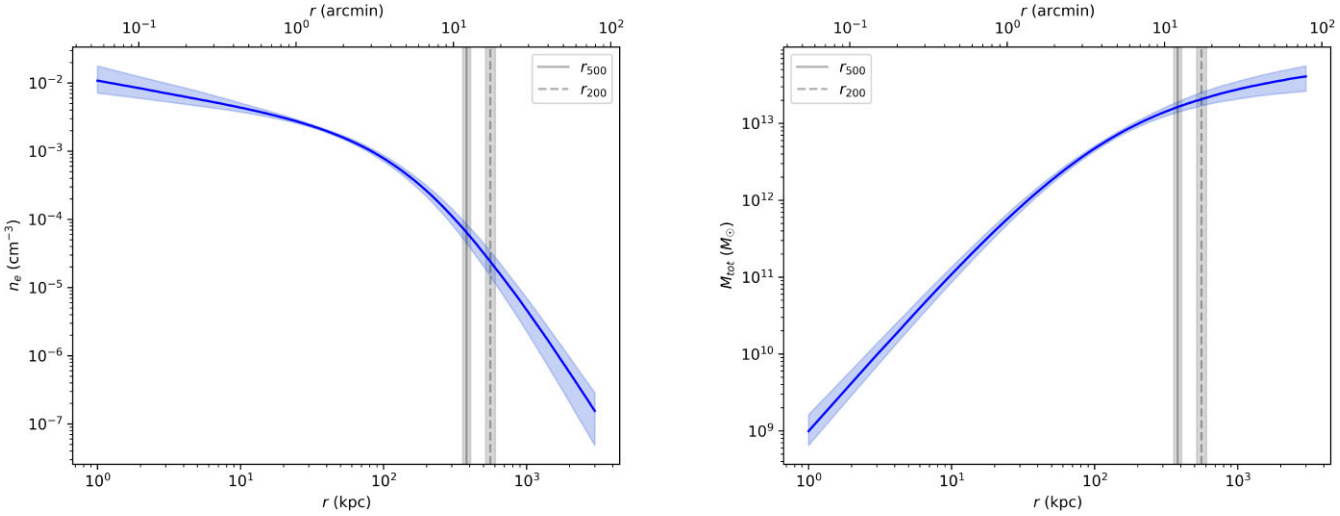

Figure 14. The distributions of the electron number density (left) and total mass (right) of the galaxy group HCG 97 using the RTI model (Zhu et al. 2016, 2021).

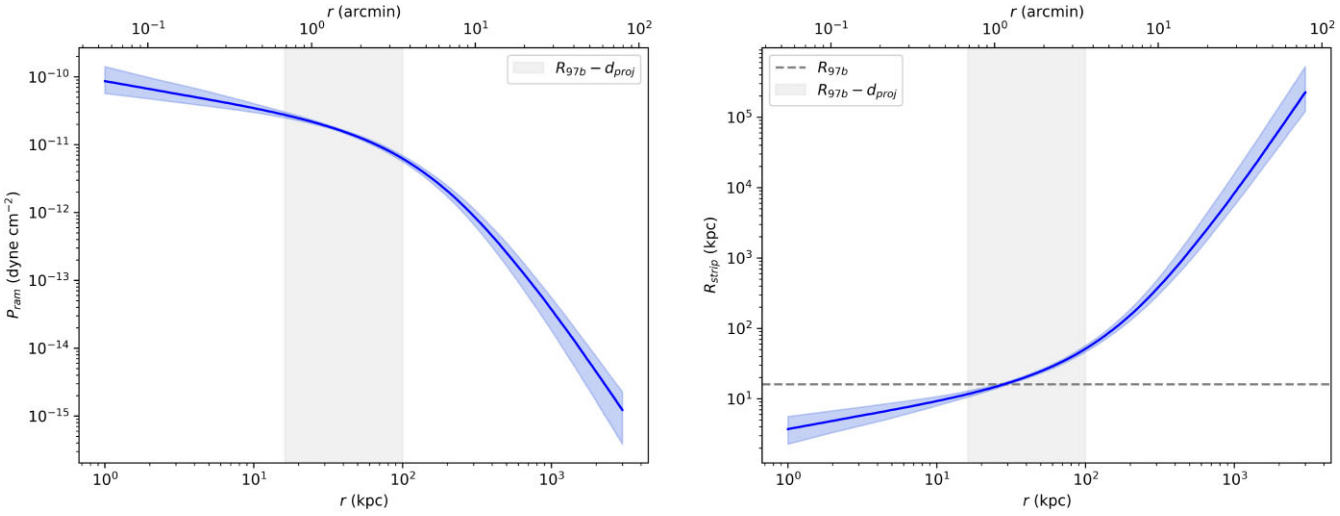

Figure 15. The ram pressure (left) and corresponding stripped radius (right) of HCG 97b as the function of the distance between the group centre and HCG 97b. The shadow region represents the range between the radius of HCG 97b (R_{97b}) and the current projected separation between the group centre and HCG 97b (d_{proj}). The radius of HCG 97b is also marked with a horizontal dash line.

the galactic nucleus in projection, i.e. ∼5.2 kpc from the galactic nucleus. Given the fact that no clear tidal tails or a significant morphological disturbance corresponding to a major merger are detected in the optical image, we speculate that X2 could be the candidate for an activated IMBH, which has encountered a dense, CO-emitting molecular gas while wandering through the galactic disc (Seepaul, Pacucci & Narayan 2022), which was originally suggested by Miller & Hamilton (2002) to interpret ULXs. There are several hypotheses about the origin of IMBHs. The IMBH could have formed within the galaxy due to a runaway merger of stellar black holes and stars (Miller & Hamilton 2002; Portegies Zwart & McMillan 2002) or it could have been captured after a minor merger with a satellite or dwarf galaxy (Weller et al. 2022). The IMBH would then subsequently undergo dynamical relaxation into the galactic plane where most molecular gas is localized within giant molecular clouds. The expected mass range is $M_{\rm BH} \sim 10^2 - 10^5$ M$_\odot$ (Greene, Strader & Ho 2020). The model of an IMBH traversing through a denser material is also supported by an increased column density of $N_{\rm H} \sim 2.3 \times 10^{22}$ cm^{-2} indicating a mild obscuration, which is consistent with the molecular gas whose column density is expected to be $\sim 10^{21} - 10^{22}$ cm^{-2} (Schneider et al. 2015), i.e. well below the Compton-thick limit of $\sim 1.5 \times 10^{24}$ cm^{-2} that would cause a severe absorption of X-ray photons. The column density is consistent with the intrinsic obscuration of the IMBH embedded inside the giant molecular cloud (GMC) of $m_{\rm GMC} \sim 10^6$ M$_\odot$ with the mean radius of $R_{\rm GMC} \sim 25$ pc,[6] which are typical parameters for a GMC (Heyer & Dame 2015). Since most of H_2 gas is contained in GMCs, we expect about $M_{\rm H_2}/m_{\rm GMC} \sim 2500$ of them in HCG 97b.

In this regard, the energy and the momentum feedback from the accretion onto the X2 source is expected to contribute to the heating and the mechanical input into the surrounding ISM, which is then

[6]The intrinsic column density then is $N_{\rm H} \sim 3 m_{\rm GMC}/(4\mu m_{\rm H} \pi R_{\rm GMC}^2) \sim 2.4 \times 10^{22}\,(m_{\rm GMC}/10^6\,{\rm M}_\odot)(R_{\rm GMC}/25\,{\rm pc})^{-2}{\rm cm}^{-2}$, where $\mu \sim 2$ is the mean molecular weight of H_2.

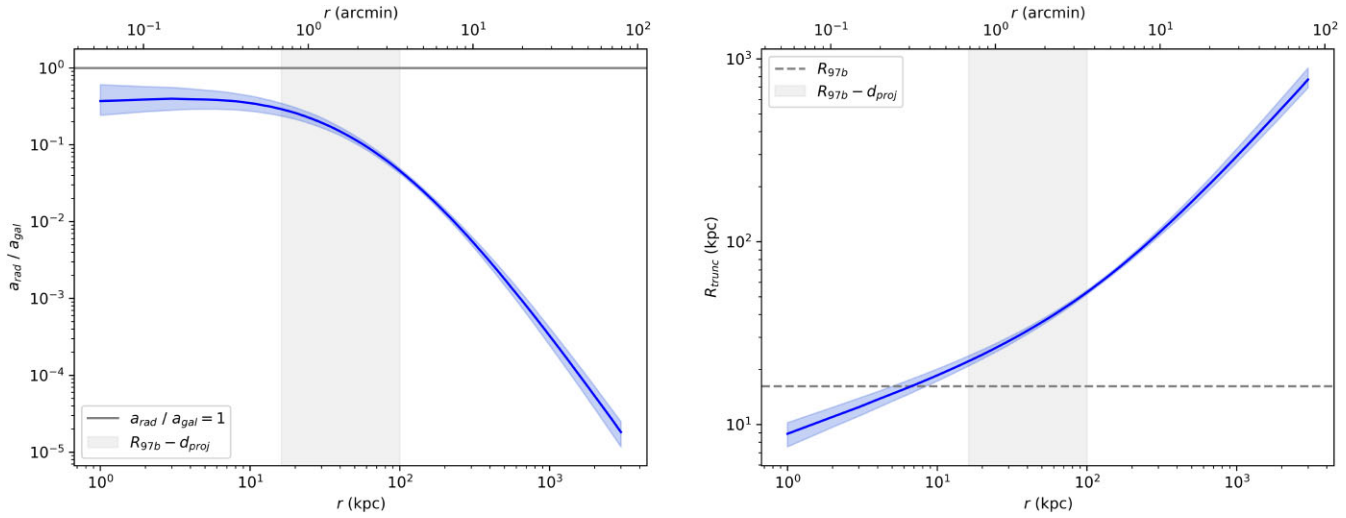

Figure 16. The ratio between the radial tidal acceleration and the internal galaxy acceleration (left) and the truncation radius (right) due to the group gravitational well as the function of the distance between the group centre and HCG 97b. The shadow region represents the range between the radius of HCG 97b (R_{97b}) and the current projected separation between the group centre and HCG 97b (d_{proj}). The radius of HCG 97b is also marked with a horizontal dash line.

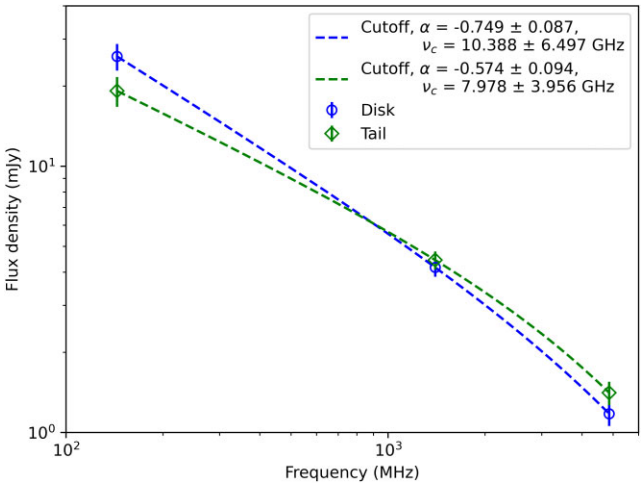

Figure 17. Radio synchrotron spectra in the disc and tail of HCG 97b after the thermal emission correction. The best fits with the exponential cut-off model are also presented.

prone to a more enhanced ram-pressure stripping. This could be relevant since the footprint of the radio tail lies in projection close to the X2 source; see Figs 4 and 6.[7] This implies a novel mechanism, in which IMBHs or ULXs in general can strengthen the ISM stripping due to the IGrM ram pressure. Such a scenario is complementary to the studied case when ram-pressure stripping ignites an AGN activity (see e.g. Peluso et al. 2022). Poggianti et al. (2017) proposed the scenario when an AGN can inject energy and momentum to enhance ram-pressure stripping, however, a potential connection with ULXs/IMBHs has not been studied. Also, currently the connection between the AGN activity and the ram-pressure stripping is unclear and some studies questioned the causal relation (see e.g. Boselli, Fossati & Sun 2022; Cattorini et al. 2023), which further motivates us to study the impact of the ULX X2 source in HCG 97b. In addition, the acceleration of electrons due to the IMBH feedback and the associated shocks can help explain the flatter spectral index of the tail region. Below we provide several analytical estimates on how this can work for typical parameters of the IMBH, ISM densities and temperatures.

Considering radiative efficiency of $\eta = 0.1$ and the bolometric correction of $\kappa_{\rm bol} = 13.3$, which is intermediate between low-luminosity and high-luminosity accretion modes (see Section 4.1), we estimate the X2 accretion rate as follows:

$$\dot{M} = \frac{L_{\rm bol}}{\eta c^2} = \frac{\kappa_{\rm bol} L_{\rm X}}{\eta c^2} \sim 4.22 \times 10^{-5} \left(\frac{\kappa_{\rm bol}}{13.3}\right) \times \left(\frac{L_{\rm X}}{1.8 \times 10^{40}\,{\rm erg\,s^{-1}}}\right) \left(\frac{\eta}{0.1}\right)^{-1} {\rm M_\odot\,yr^{-1}}, \quad (11)$$

where $L_{\rm X} = 1.8 \times 10^{40}$ erg s^{-1} is the 2–10 keV luminosity of the X2 source. The accretion rates of the order of $\dot{M}$ given by equation (11) are consistent with the passages of IMBHs through molecular clouds as studied by Seepaul, Pacucci & Narayan (2022), who predicted X-ray luminosities exceeding 10^{41} erg s^{-1} for the brightest cases. Considering the whole range of IMBH masses, $M_{\rm BH} \sim 10^2 - 10^5\,{\rm M_\odot}$, the Eddington ratio is in the range of $\lambda_{\rm Edd} = \dot{M}/\dot{M}_{\rm Edd} \sim 0.02 - 19.1$, where the larger values correspond to smaller IMBH masses. Since the IMBH coincides with the CO emission peak and we assume that it is fueled by the accretion from the surrounding molecular gas, a quasispherical thick hot flow with a lower Eddington ratio is expected to develop (Seepaul, Pacucci & Narayan 2022). Such a Bondi-like flow has properties similar to ADAF and is also associated with powerful outflows that could have contributed to the radio-tail development via their mechanical feedback, or at least they increased the amount of gas escaping from the host galaxy in addition to the IGrM ram pressure.

Therefore, for the following estimates, assuming the ADAF and the IMBH mass range, we fix the Eddington ratio to $\lambda_{\rm Edd} = 10^{-2}$, which implies the IMBH mass of $M_{\rm BH} \sim 3.5 \times 10^5$ M$_\odot$. This set-up is also consistent with the assumed radiative efficiency of $\eta \sim 0.1$ (Yuan & Narayan 2014). To model the accretion from the CO-emitting gas, we consider the Bondi–Hoyle–Lyttleton (BHL)-like accretion from the molecular cloud with the H_2 number density

[7]Previously, the jellyfish galaxy JW100 was also reported to host a bright ULX source; however, it does not have any apparent connection with the observed radio tail (Poggianti et al. 2019)

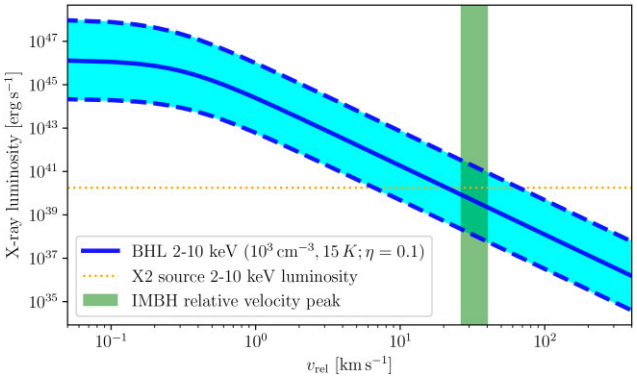

Figure 18. The 2–10 keV luminosities corresponding to the BHL accretion as a function of the relative velocity of a wandering IMBH with respect to the galactic disc molecular gas (solid line; the ambient molecular cloud has a number density of 10^3 cm^{-3} and temperature of 15 K). The inferred X-ray luminosity of the X2 source is denoted by the **horizontal** dotted line. The **shaded** area and dashed lines express the BHL X-ray luminosities for the whole range of the molecular cloud characteristic parameters (number densities of $10^2 - 10^4$ cm^{-3} and temperatures of $10 - 20$ K). The vertical rectangle represents the estimated peak of the IMBH relative velocity distribution with respect to the local gas inferred from the Illustris TNG50 simulations (Seepaul, Pacucci & Narayan 2022).

range of $n_{\rm MC} \sim 10^2 - 10^4$ cm^{-3} and the ambient temperature of $T_{\rm MC} \sim 10 - 20$ K (Seepaul, Pacucci & Narayan 2022), which fixes the ambient mass density ρ and the ambient gas sound speed $c_{\rm s}$. Following the basic BHL accretion theory, the accretion rate at the outer radius $R_{\rm A}$ is given by (see e.g. Seepaul, Pacucci & Narayan 2022, and references therein),

$$\dot{M}_{\rm B} = \frac{4\pi G^2 M_{\rm BH}^2 \rho}{(v_{\rm rel}^2 + c_{\rm s}^2)^{3/2}}, \tag{12}$$

where $v_{\rm rel}$ is the relative velocity of the IMBH with respect to the local molecular gas. Due to the powerful outflows and conduction, the actual gas inflow rate through the IMBH horizon is scaled down with respect to $\dot{M}_{\rm B}$ following a simple power-law relation,

$$\dot{M}_{\rm in} \sim \dot{M}_{\rm B} \left(\frac{R_{\rm in}}{R_{\rm A}}\right)^p, \tag{13}$$

where the effective inner radius of the flow is set to $R_{\rm in} = 50R_{\rm S}$ (Abramowicz et al. 2002), with $R_{\rm S} = 2GM_{\rm BH}/c^2$ being the Schwarzschild radius. The outer radius is given by the gravitational capture radius $R_{\rm A} = 2GM_{\rm BH}/(v_{\rm rel}^2 + c_{\rm s}^2)$. The power-law slope in equation (13) is set to $p = 0.5$, which is motivated by numerical calculations of hot flows (Yuan & Narayan 2014; Ressler et al. 2020).

To determine the required relative velocity $v_{\rm rel}$, we compare $\dot{M}_{\rm in}$, or rather the corresponding X-ray luminosity $L_{\rm X} \sim \eta \dot{M}_{\rm in} c^2/\kappa_{\rm bol}$ with the inferred 2–10 keV luminosity of X2. From Fig. 18, we see that to reproduce the X2 X-ray luminosity, the IMBH is expected to move at the relative velocity of $\sim 6.6 - 66.3$ km s^{-1} with respect to the local molecular gas, with $v_{\rm rel} \sim 21$ km s^{-1} corresponding to the intermediate number density of 10^3 cm^{-3} and the temperature of 15 K. This interval is consistent with the peak of the IMBH velocity distribution with respect to the surrounding gas inferred from Illustris TNG50 simulations (Seepaul, Pacucci & Narayan 2022; Weller et al. 2022), which is in the range of $26 - 41$ km s^{-1}.

We further estimate if the activated IMBH of $M_{\rm BH} \sim 3.4 \times 10^5$ M$_\odot$ can significantly impact the surrounding molecular gas and induce the formation of the radio tail structure. The traversing IMBH crosses a typical molecular cloud in $\tau_{\rm cross} = D_{\rm MC}/v_{\rm rel} \sim 4.66 \times 10^5$ yr for the molecular cloud diameter of $D_{\rm MC} \sim 10$ pc (Heyer & Dame 2015) and the relative velocity of $v_{\rm rel} \simeq 21$ km s^{-1} (see the estimate above). During $\tau_{\rm cross}$, the ADAF flow surrounding the IMBH generates a significant outflow and potentially a relativistic jet that impacts the surrounding ISM via mechanical feedback as well as radiation pressure both from the accretion as well as the generated shocks when the outflow impacts the molecular cloud (see e.g. Ferrara & Scannapieco 2016; Goicoechea et al. 2016). The observed 27-kpc radio tail of HCG 97b could have thus been formed and shaped via:

(i) jet generated in the inner zone of the ADAF where the outflowing plasma is collimated by the ordered magnetic field and can reach ultrafast velocities in excess of 0.1c (see e.g. Suková et al. 2021), which is further distorted by the IGrM ram pressure,

(ii) uplift of the ISM material due to IMBH-induced mechanical feedback and subsequent IGrM ram-pressure prolongation and distortion.

The radio tail generation with the case (i) scenario can work if the inner ADAF surrounding the IMBH can support the ultrafast outflow/jet with the velocity of $v_{\rm UFO} \sim D_{\rm tail}/\tau_{\rm cross} \sim 0.2$ c to be able to create the tail of the 27-kpc length during the crossing time. The restriction on the jet outflow velocity can be eased if the IMBH is fed by the molecular material for a longer duration than inferred from the typical cloud size. The scenario where radio jet is generated by an accreting IMBH is also supported by the recent detection of the two-sided jet ($L_{1.66\ \rm GHz} \sim 3 \times 10^{38}$ erg s^{-1}) associated with the IMBH of 3.6×10^5 M$_\odot$ in a dwarf galaxy (Yang et al. 2023). At 1.4 GHz, the tail luminosity of HCG 97b is comparable to that value, $L_{1.4\ \rm GHz} \sim 7 \times 10^{37}$ erg s^{-1} within an order of magnitude. The one-sided nature of the IMBH jet outflow, which could be associated with the north-western radio lobe visible at 4.86 GHz, can be caused by a small viewing angle and/or the distortion, bending, and further prolongation of the tail by the IGrM ram pressure. In this picture, the extended tail part could be the remnant of the previous accretion activity of the X2 as it passed through another denser molecular-cloud core. This scenario provides a possible explanation of the high velocity of the radio plasma in the radio tail, as discussed in Section 4.2.3, and can be further studied by observing a small-scale radio emission associated with the X-ray point source X2. Furthermore, the flatter radio spectral index inferred for the tail can be interpreted as a result of the local electron acceleration process, such as in shocks created due to the interaction between the jet launched by the IMBH and the IGrM.

Case (ii) can be supported by comparing the mechanical energy density of the generated wide-angle outflow $\epsilon_{\rm out}$ with the thermal energy density of the surrounding gas $\epsilon_{\rm gas} \sim \rho c_{\rm s}^2$. The outflow rate for the ADAF $\dot{M}_{\rm out}$ is much larger than the inflow rate $\dot{M}_{\rm in}$ and can be expressed as $\dot{M}_{\rm out} = \dot{M}_{\rm B}[1 - (R_{\rm in}/R_{\rm A})]^p$, which results in $\dot{M}_{\rm out} \sim 0.16$ M$_\odot$ yr^{-1} or about 2024 times more than the inflow rate for the intermediate molecular-cloud number density of 10^3 cm^{-3}. The hot outflow velocity is estimated using $v_{\rm out} = 0.2 v_{\rm K}(R_{\rm A}) \sim 3$ km s^{-1} (Yuan et al. 2018), where $v_{\rm K}(R_{\rm A}) \sim 14.8$ km s^{-1} is the Keplerian velocity at $R_{\rm A} \sim 6.86$ pc. The hot outflow energy density can then be estimated as

$$\epsilon_{\rm out} \sim \frac{1}{2}\frac{\dot{M}_{\rm out}}{V_{\rm MC}} \tau_{\rm cross} v_{\rm out}^2 = \frac{1}{2}\frac{\dot{M}_{\rm out} v_{\rm out}^2}{D_{\rm MC}^2 v_{\rm rel}} \sim 2.3 \times 10^{-10} \rm erg\,cm^{-3} \tag{14}$$

where $V_{\rm MC} \sim D_{\rm MC}^3$ is the molecular cloud volume. We compare $\epsilon_{\rm out}$ with the thermal energy density of the molecular gas, $\epsilon_{\rm gas} \sim n_{\rm gas} k_{\rm B} T_{\rm gas} \sim 2.1 \times 10^{-12}$ erg cm^{-3}, as well as with that of the radio-emitting warm and hot ionized plasma, $\epsilon_{\rm gas} \sim (0.3\,\rm cm^{-3}) \times$

$(1.38 \times 10^{-16}\,\mathrm{erg\,K^{-1}}) \times 9000\,\mathrm{K} \sim 3.7 \times 10^{-13}\,\mathrm{erg\,cm^{-3}}$ and $\epsilon_{\rm gas} \sim (3 \times 10^{-3}\,\mathrm{cm^{-3}}) \times (1.38 \times 10^{-16}\,\mathrm{erg\,K^{-1}}) \times (5 \times 10^{6}\,\mathrm{K}) \sim 2.1 \times 10^{-12}\,\mathrm{erg\,cm^{-3}}$, respectively (see e.g. Seepaul, Pacucci & Narayan 2022), and we see that $\epsilon_{\rm out}$ is larger by two-three orders of magnitude. In order for the gas to escape from the galaxy, $\epsilon_{\rm out}$ needs to be larger than the gravitational binding energy density $\epsilon_{\rm bind}$. For a more diluted ionized gas in the warm-hot ISM, we estimate $\epsilon_{\rm bind}$ assuming the virial theorem and using the mean rotational velocity $v_{\rm rot} \sim 218\,\mathrm{km\,s^{-1}}$ (see Section 3.3),

$$\epsilon_{\rm bind} \sim \frac{1}{2}\frac{M_{\rm gas}}{V_{\rm gas}} v_{\rm rot}^2 \sim \frac{1}{2}\rho_{\rm gas} v_{\rm rot}^2 \sim 4 \times 10^{-11} \left(\frac{n_{\rm gas}}{0.1\,\mathrm{cm^{-3}}}\right) \left(\frac{v_{\rm rot}}{218\,\mathrm{km\,s^{-1}}}\right)^2 \mathrm{erg\,cm^{-3}}, \quad (15)$$

which is smaller than $\epsilon_{\rm out}$ for typical warm/hot ionized medium number densities. Overall, this would lead to the uplift of gas and its subsequent easier stripping by the ram pressure of the IGrM. Currently, only the radio tail tracing the ionized plasma is observed. Future more sensitive observations, e.g. Hα + [N II] narrow band imaging, will constrain the amount of the stripped neutral gas. However, the mechanical uplifting of the galactic ISM gas works more efficiently for the less dense ionized component, which follows from the comparison of equations (15) and (14). This can explain the lack of the neutral and molecular gas in the ram-pressure stripped tail since it rather stays within the galactic disc due to larger binding energy.

The lower-Eddington ratio ADAF model for the X2 X-ray emission is motivated by the plausible accretion from the ISM (Seepaul, Pacucci & Narayan 2022). The Bondi-like hot flow is also associated with a non-thermal radio emission due to the ADAF spectral energy distribution (Yuan & Narayan 2014). Moreover, a wide-angle outflow is naturally generated; hence, mechanical feedback could contribute to the detected stripped material.

If instead, the accretion of the ambient dense gas proceeds with an Eddington ratio close to unity, and hence in the radiatively efficient mode, the X2 mass would be pushed to lower values, though still in the IMBH mass range,

$$M_{\rm BH} \simeq 300.4 \left(\frac{L_{\rm X}}{1.8 \times 10^{40}\,\mathrm{erg\,s^{-1}}}\right)^{1.3} \left(\frac{\lambda_{\rm Edd}}{1}\right)^{-1} \mathrm{M_\odot}, \quad (16)$$

which follows from equation (4), where we express the bolometric correction $\kappa_{\rm bol}$ following Netzer (2019) ($\kappa_{\rm bol} \sim 2.1$ for the X2 2–10 keV luminosity) and hence the standard disc formalism. We note that the Eddington limit would have to be exceeded by a factor of at least 3 for the X2 to reach stellar-mass black hole masses and the neutron-star mass range would be reached for $\lambda_{\rm Edd} \sim 200$ (see Table 3 for the BH mass-range estimates for the Eddington ratio between 10^{-2} and 10^{2}). For $\lambda_{\rm Edd} \sim 1$, the accretion flow has the structure of a geometrically and optically thick slim disc (Abramowicz et al. 1988) or a 'puffy' disc (Lančová et al. 2019), for which radiation-driven outflows are expected (Feng et al. 2019). Since the outflow is radiatively driven, we can estimate the radiative feedback to the surrounding medium from the bolometric accretion luminosity, assuming the efficient mode during the whole passage of the IMBH through the molecular cloud,

$$\epsilon_{\rm rad} \sim \frac{\kappa_{\rm bol} L_{\rm X} \tau_{\rm cross}}{D_{\rm MC}^3} = \frac{\kappa_{\rm bol} L_{\rm X}}{D_{\rm MC}^2 v_{\rm rel}} \sim 1.9 \times 10^{-5}\,\mathrm{erg\,cm^{-3}}, \quad (17)$$

where we assumed that the released radiative energy during $\tau_{\rm cross}$ is primarily impacted within the molecular cloud volume. We see that $\epsilon_{\rm rad}$ is larger than typical gas thermal energy and binding energy densities $\epsilon_{\rm gas}$ and $\epsilon_{\rm bin}$ estimated previously by several orders of magnitude, hence the radiative feedback expected from a lower-mass IMBH or a stellar-mass BH is expected to have profound effects on the surrounding molecular gas, which should result in the severe disturbance and uplifting of bound gas. In this case, we would expect a harder X-ray emission due to a smaller black-hole mass, which would result in the ionization of the neutral and molecular gas that is observationally not detected in the tail of HCG 97b.

More constraints on the X2 mass will follow from the future detailed X-ray spectroscopy and timing, which will also help clarify the accretion mode and the type of feedback. In addition, magnetohydrodynamical simulations may be necessary to fully capture the interaction between the IMBH-generated outflow and the ISM medium, as well as the IGrM ram pressure, which is beyond the scope of the current study.

Given that HCG 97b is slightly larger than the Milky Way, both X2 and X1 X-ray sources are located relatively in the central regions of HCG 97b, i.e. within ∼5.2 kpc from the nucleus, where the occurrences of both the molecular gas and IMBHs are statistically increased, and hence also the probability of their interaction (Heyer & Dame 2015; Seepaul, Pacucci & Narayan 2022; Weller et al. 2022). The X1 source could also be the candidate for an IMBH with ∼0.86 kpc offset from the nucleus, though its location does not coincide with the CO emission peak, which is supported by the smaller obscuration in comparison with X2. Therefore X1 is not a prime candidate for a wandering IMBH reactivated by the interaction with the molecular gas (Seepaul, Pacucci & Narayan 2022). The constrained steeper power-law index ($\Gamma = 2.65 \pm 0.87$; Section 3.1) of X1 indicates a soft state and a higher Eddington ratio, which makes it a candidate for a stellar-mass ULX with the mass of ∼39.5 $\mathrm{M_\odot}$ for the Eddington limit.

5 CONCLUSIONS

In this paper, we present a multiwavelength analysis of the spiral galaxy HCG 97b, and the main results are summarized as follows:

(i) *LOFAR* 144 MHz, *VLA* 1.4 GHz and 4.86 GHz images reveal asymmetric, extended radio continuum emission of the spiral galaxy HCG 97b, including an elongated radio emission along the optical disc and an extraplanar, one-sided radio tail extending ∼27 kpc toward the group centre at GHz frequencies and to ∼60 kpc at 144 MHz.

(ii) Chandra images reveal two off-centre X-ray sources with 2–10 keV luminosities of $\sim 10^{39} - 10^{40}\,\mathrm{erg\,s^{-1}}$. Given the off-nuclear location and the observed X-ray luminosity, these two X-ray sources are most likely ULXs.

(iii) The source X2 is a suitable candidate for an accreting IMBH embedded in an environment with an increased density of molecular gas.

(iv) Asymmetry in the molecular gas within the disc is evident from both CO emission morphology and kinematics, indicating that HCG 97 is experiencing ram-pressure stripping, with the leading side at the south-eastern edge of the disc.

(v) Based on estimations of the capabilities of gravitational and hydrodynamic processes, it seems HCG 97b has experienced gravitational interaction and is currently subjected to ram pressure stripping. Both mechanisms have played roles in gas stripping, with the gravitational interaction potentially flattening the galaxy's gravitational potential well, making the gaseous components of the galaxy more susceptible to being stripped away by ram pressure.

(vi) The *VLA* 4.86 GHz image reveals two bright radio blobs – one above the disc and another outside of it, aligning with the

radio tail. Their proximity to source X2, along with comparable and flat spectra indices ($\alpha > -1$) in the disc and tail, suggests that these blobs may be a pair of radio lobes recently powered by ULX feedback.

(vii) Considering the radiative time of CRe in the tail is 2.2×10^7 yr, the expected velocity needed for transporting CRe from the disc to the tail is approximately 1300 km s^{-1}. This velocity substantially exceeds those observed in other ram-pressure stripped galaxies ($100 - 600$ km s^{-1}; Ignesti et al. 2023), and aligns with velocities found in head-tail radio galaxies (Ignesti et al. 2020; Edler et al. 2022). Therefore, the formation of the radio tail might also be influenced by the putative IMBH-induced activity.

ACKNOWLEDGEMENTS

We sincerely thank the referee for providing valuable comments and suggestions. We thank Chentao Yang, Junjie Mao, Stefan William Duchesne, and Muryel Guolo for their valuable assistance and helpful discussion. This research was supported by the GACR grant 21–13491X. DH acknowledges the National Science Foundation of China (grant No. 12233005). RG acknowledges support from the project LM2018106 of the Ministry of Education, Youth and Sports of the Czech Republic and project RVO:67985815. AI acknowledges funding from the European Research Council (ERC) under the European Union's Horizon 2020 research and innovation programme (grant agreement No. 833824 and the INAF founding program 'Ricerca Fondamentale 2022' (PI A Ignesti). ZZ acknowledges support from the National Science Foundation of China (grant No. 12203085).

We acknowledge the use of the Legacy Surveys data and the Helpdesk for guidance in generating a composite DECaLS image.

DATA AVAILABILITY

The data in this article are available on request to the corresponding author.

REFERENCES

Abramowicz M. A., Czerny B., Lasota J. P., Szuszkiewicz E., 1988, ApJ, 332, 646
Abramowicz M. A., Igumenshchev I. V., Quataert E., Narayan R., 2002, ApJ, 565, 1101
Basu A., Beck R., Schmidt P., Roy S., 2015, MNRAS, 449, 3879
Behroozi P. S., Wechsler R. H., Conroy C., 2013, ApJ, 770, 57
Bharadwaj V., Reiprich T. H., Schellenberger G., Eckmiller H. J., Mittal R., Israel H., 2014, A&A, 572, A46
Bigiel F., Leroy A., Walter F., Brinks E., de Blok W. J. G., Madore B., Thornley M. D., 2008, AJ, 136, 2846
Bitsakis T., Charmandaris V., da Cunha E., Díaz-Santos T., Le Floc'h E., Magdis G., 2011, A&A, 533, A142
Bizyaev D. V., Kautsch S. J., Mosenkov A. V., Reshetnikov V. P., Sotnikova N. Y., Yablokova N. V., Hillyer R. W., 2014, ApJ, 787, 24
Boselli A., Fossati M., Sun M., 2022, A&A Rev., 30, 3
Briggs D. S., 1995, PhD thesis, New Mexico Institute of Mining and Technology
Buchner J. et al., 2014, A&A, 564, A125
Byrd G., Valtonen M., 1990, ApJ, 350, 89
Cattorini F., Gavazzi G., Boselli A., Fossati M., 2023, A&A, 671, A118
Chen H. et al., 2020, MNRAS, 496, 4654
Chung A., van Gorkom J. H., Kenney J. D. P., Vollmer B., 2007, ApJ, 659, L115
Chung A., van Gorkom J. H., Kenney J. D. P., Crowl H., Vollmer B., 2009, AJ, 138, 1741
Condon J. J., 1992, ARA&A, 30, 575
Cortese L. et al., 2007, MNRAS, 376, 157
Cramer W. J., Kenney J. D. P., Cortes J. R., Cortes P. C., Vlahakis C., Jáchym P., Pompei E., Rubio M., 2020, ApJ, 901, 95
Cramer W. J. et al., 2023, ApJ, 944, 213
d'Antonio D., Giroletti M., Giovannini G., Maini A., 2019, MNRAS, 490, 5798
den Brok J. S. et al., 2021, MNRAS, 504, 3221
den Brok J. S. et al., 2023, A&A, 676, A93
Davis D. S., Keel W. C., Mulchaey J. S., Henning P. A., 1997, AJ, 114, 613
Deb T. et al., 2020, MNRAS, 494, 5029
Dey A. et al., 2019, AJ, 157, 168
Dong A.-J., Wu Q., Cao X.-F., 2014, ApJ, 787, L20
Ebeling H., Stephenson L. N., Edge A. C., 2014, ApJ, 781, L40
Edler H. W. et al., 2022, A&A, 666, A3
Feng J., Cao X., Gu W.-M., Ma R.-Y., 2019, ApJ, 885, 93
Ferrara A., Scannapieco E., 2016, ApJ, 833, 46
Fumagalli M., Fossati M., Hau G. K. T., Gavazzi G., Bower R., Sun M., Boselli A., 2014, MNRAS, 445, 4335
Gavazzi G., Jaffe W., 1987, A&A, 186, L1
Gavazzi G., Boselli A., Mayer L., Iglesias-Paramo J., Vílchez J. M., Carrasco L., 2001, ApJ, 563, L23
Gavazzi G., Consolandi G., Yagi M., Yoshida M., 2017, A&A, 606, A131
Goicoechea J. R. et al., 2016, Nature, 537, 207
Goodwin S. P., Gribbin J., Hendry M. A., 1998, Observatory, 118, 201
Greene J. E., Strader J., Ho L. C., 2020, ARA&A, 58, 257
Grossová R. et al., 2022, ApJS, 258, 30
Gültekin K., King A. L., Cackett E. M., Nyland K., Miller J. M., Di Matteo T., Markoff S., Rupen M. P., 2019, ApJ, 871, 80
Gunn J. E., Gott J. R. I., 1972, ApJ, 176, 1
HI4PI Collaboration, 2016, A&A, 594, A116
Hale C. L. et al., 2019, A&A, 622, A4
Healey S. E., Romani R. W., Taylor G. B., Sadler E. M., Ricci R., Murphy T., Ulvestad J. S., Winn J. N., 2007, ApJS, 171, 61
Henriksen M., Byrd G., 1996, ApJ, 459, 82
Heyer M., Dame T. M., 2015, ARA&A, 53, 583
Hickson P., Mendes de Oliveira C., Huchra J. P., Palumbo G. G., 1992, ApJ, 399, 353
Hu D. et al., 2021, ApJ, 913, 8
Ignesti A. et al., 2020, A&A, 643, A172
Ignesti A. et al., 2022, ApJ, 924, 64
Ignesti A. et al., 2023, A&A, 675, A118
Jáchym P., Combes F., Cortese L., Sun M., Kenney J. D. P., 2014, ApJ, 792, 11
Jáchym P. et al., 2019, ApJ, 883, 145
Jones M. G. et al., 2023, A&A, 670, A21
Kaaret P., Feng H., Roberts T. P., 2017, ARA&A, 55, 303
Kantharia N. G., Ananthakrishnan S., Nityananda R., Hota A., 2005, A&A, 435, 483
Kenney J. D. P., Tal T., Crowl H. H., Feldmeier J., Jacoby G. H., 2008, ApJ, 687, L69
Kenney J. D. P., Geha M., Jáchym P., Crowl H. H., Dague W., Chung A., van Gorkom J., Vollmer B., 2014, ApJ, 780, 119
Klein U., Lisenfeld U., Verley S., 2018, A&A, 611, A55
Koopmann R. A., Kenney J. D. P., 2004, ApJ, 613, 866
Lančová D. et al., 2019, ApJ, 884, L37
Lee B. et al., 2017, MNRAS, 466, 1382
Leroy A. K. et al., 2013, AJ, 146, 19
Łokas E. L., 2020, A&A, 638, A133
Longair M. S., 2011, High Energy Astrophysics. Cambridge Univ. Press, Cambridge
Machacek M. E., Nulsen P., Stirbat L., Jones C., Forman W. R., 2005, ApJ, 630, 280
McMullin J. P., Waters B., Schiebel D., Young W., Golap K., 2007, in Shaw R. A., Hill F., Bell D. J., eds, ASP Conf. Ser. Vol. 376, Astronomical Data Analysis Software and Systems XVI. Astron. Soc. Pac., San Francisco. p. 127

Makarov D., Prugniel P., Terekhova N., Courtois H., Vauglin I., 2014, A&A, 570, A13
Martinez-Badenes V., Lisenfeld U., Espada D., Verdes-Montenegro L., García-Burillo S., Leon S., Sulentic J., Yun M. S., 2012, A&A, 540, A96
Massaro F., Giroletti M., D'Abrusco R., Masetti N., Paggi A., Cowperthwaite P. S., Tosti G., Funk S., 2014, ApJS, 213, 3
Mayer L., Mastropietro C., Wadsley J., Stadel J., Moore B., 2006, MNRAS, 369, 1021
Merloni A., Heinz S., di Matteo T., 2003, MNRAS, 345, 1057
Mihos J. C., Hernquist L., 1994a, ApJ, 425, L13
Mihos J. C., Hernquist L., 1994b, ApJ, 431, L9
Miley G., 1980, ARA&A, 18, 165
Miller M. C., Hamilton D. P., 2002, MNRAS, 330, 232
Misquitta P., Eckart A., Zajaček M., Yttergren M., 2023, A&A, 671, A18
Müller A. et al., 2021, Nat. Astron., 5, 159
Murphy E. J., Kenney J. D. P., Helou G., Chung A., Howell J. H., 2009, ApJ, 694, 1435
Nemmen R. S., Storchi-Bergmann T., Eracleous M., 2014, MNRAS, 438, 2804
Netzer H., 2019, MNRAS, 488, 5185
Nulsen P. E. J., 1982, MNRAS, 198, 1007
Offringa A. R. et al., 2014, MNRAS, 444, 606
Oman K. A., Bahé Y. M., Healy J., Hess K. M., Hudson M. J., Verheijen M. A. W., 2021, MNRAS, 501, 5073
Peluso G. et al., 2022, ApJ, 927, 130
Perley R. A., Butler B. J., 2017, ApJS, 230, 7
Plotkin R. M., Markoff S., Kelly B. C., Körding E., Anderson S. F., 2012, MNRAS, 419, 267
Poggianti B. M. et al., 2017, Nature, 548, 304
Poggianti B. M. et al., 2019, ApJ, 887, 155
Portegies Zwart S. F., McMillan S. L. W., 2002, ApJ, 576, 899
Quilis V., Moore B., Bower R., 2000, Science, 288, 1617
Rasmussen J., Ponman T. J., Mulchaey J. S., 2006, MNRAS, 370, 453
Rasmussen J., Ponman T. J., Verdes-Montenegro L., Yun M. S., Borthakur S., 2008, MNRAS, 388, 1245
Ressler S. M., White C. J., Quataert E., Stone J. M., 2020, ApJ, 896, L6
Roberts I. D. et al., 2021a, A&A, 650, A111
Roberts I. D., van Weeren R. J., McGee S. L., Botteon A., Ignesti A., Rottgering H. J. A., 2021b, A&A, 652, A153
Roberts I. D., van Weeren R. J., Timmerman R., Botteon A., Gendron-Marsolais M., Ignesti A., Rottgering H. J. A., 2022a, A&A, 658, A44
Roberts I. D. et al., 2022b, ApJ, 941, 77
Roediger E. et al., 2015, ApJ, 806, 104
Sardaneta M. M. et al., 2022, A&A, 659, A45
Schneider N. et al., 2015, A&A, 578, A29
Seepaul B. S., Pacucci F., Narayan R., 2022, MNRAS, 515, 2110
Shimwell T. W. et al., 2017, A&A, 598, A104
Shimwell T. W. et al., 2022, A&A, 659, A1
Sivakoff G. R., Sarazin C. L., Carlin J. L., 2004, ApJ, 617, 262
Smith R. J. et al., 2010, MNRAS, 408, 1417
Solomon P. M., Vanden Bout P. A., 2005, ARA&A, 43, 677
Spitzer Lyman J., Baade W., 1951, ApJ, 113, 413
Springel V., 2000, MNRAS, 312, 859
Suková P., Zajaček M., Witzany V., Karas V., 2021, ApJ, 917, 43
Sun M., Jones C., Forman W., Nulsen P. E. J., Donahue M., Voit G. M., 2006, ApJ, 637, L81
Sun M., Donahue M., Voit G. M., 2007, ApJ, 671, 190
Sun M., Donahue M., Roediger E., Nulsen P. E. J., Voit G. M., Sarazin C., Forman W., Jones C., 2010, ApJ, 708, 946
Tabatabaei F. S. et al., 2017, ApJ, 836, 185
Tasse C., 2014, A&A, 566, A127
Tasse C. et al., 2018, A&A, 611, A87
Valluri M., 1993, ApJ, 408, 57
van Diepen G., Dijkema T. J., Offringa A., 2018, Astrophysics Source Code Library, record ascl:1804.003
van Weeren R. J. et al., 2021, A&A, 651, A115
Vollmer B., 2003, A&A, 398, 525
Vollmer B., Beck R., Kenney J. D. P., van Gorkom J. H., 2004, AJ, 127, 3375
Vollmer B., Soida M., Chung A., Chemin L., Braine J., Boselli A., Beck R., 2009, A&A, 496, 669
Vollmer B., Soida M., Beck R., Chung A., Urbanik M., Chyży K. T., Otmianowska-Mazur K., Kenney J. D. P., 2013, A&A, 553, A116
Vollmer B. et al., 2021, A&A, 645, A121
Wang S., Liu J., Qiu Y., Bai Y., Yang H., Guo J., Zhang P., 2016, ApJS, 224, 40
Weller E. J., Pacucci F., Hernquist L., Bose S., 2022, MNRAS, 511, 2229
Yang J. et al., 2023, MNRAS, 520, 5964
Yuan F., Narayan R., 2014, ARA&A, 52, 529
Yuan F., Yoon D., Li Y.-P., Gan Z.-M., Ho L. C., Guo F., 2018, ApJ, 857, 121
Zhu Z. et al., 2016, ApJ, 816, 54
Zhu Z. et al., 2021, ApJ, 908, 17

This paper has been typeset from a TEX/LATEX file prepared by the author.